Journal of Alloys and Compounds 768 (2018) 298–315

Contents lists available at ScienceDirect

Journal of Alloys and Compounds

journal homepage: http://www.elsevier.com/locate/jalcom

Effects of deposition method and conditions for IGZO film and thermal annealing on composite film quality, surface roughness, microstructural defects, and electrical properties of Ti/IGZO/graphene/polyimide specimens

Chang-Shuo Chang [a, c, **], Tse-Chang Li [a], Yi-Chan Tsai [a], Gien-Huang Wu [a], Jen-Fin Lin [a, b, *]

[a] Department of Mechanical Engineering, National Cheng Kung University, Tainan 701, Taiwan
[b] Center for Micro/Nano Science and Technology, National Cheng Kung University, Tainan 701, Taiwan
[c] Department of Aviation and Communication Electronics, Air Force Institute of Technology, Kaohsiung 820, Taiwan

ARTICLE INFO

Article history:
Received 8 January 2018
Received in revised form
19 July 2018
Accepted 22 July 2018
Available online 24 July 2018

Keywords:
Radio-frequency (RF) magnetron sputtering
E-beam evaporation
Indium gallium zinc oxide
Rapid thermal annealing (RTA)
Electrical and mechanical properties

ABSTRACT

The depositions of a thin graphene as the inter layer of the indium gallium zinc oxide (IGZO) film and polyimide substrate and a Ti film bellow the IGZO layer to induce the IGZO crystallizations have been reported by the authors' study [1] to have a significant reduction in the electrical resistivity (R) and increases in carrier mobility (M_b) and concentration (C_c) via the annealing as compared to those created in the specimens without graphene. In the present study, Ti/IGZO/graphene/polyimide specimens were fabricated using Ti as the top layer, with the IGZO film prepared using e-beam evaporation and radio-frequency magnetron sputtering, in order to compare the ability of preserving the structure integrity of graphene after the IGZO deposition. When sputtering was used, the thicknesses of the Ti and IGZO films were controlled by the deposition power; when e-beam evaporation was used, the thicknesses were controlled by the deposition time. Rapid thermal annealing (RTA) was further applied to some specimens to investigate the combined effects of the IGZO deposition method and heat treatment on the microstructure defects, electrical and mechanical properties, and surface morphology of the specimens. The quantities of bulges and microvoid defects increase after the RTA, and become the governing factors for increasing surface roughness (R_a). The X-ray photoelectron spectroscopy spectra for O1s were deconvoluted to evaluate the peak intensity ratio, IR_{O2}, defined for the evaluation of the oxygen vacancies in the microstructure. When sputtering was used, IR_{O2} increased after RTA; in contrast, when e-beam evaporation was used, IR_{O2} decreased after RTA. For all specimens without RTA, an increase in either the deposition power or time of IGZO has decreased IR_{O2}. TiO_2, ZnO, and Ga_2O_3 are the three oxides created in the specimens. The ways of increasing the TiO_2 grains result in a rise of IR_{O2}. The electrons released from the TiO_2 formations are available to raise the quantity of ZnO. The peak intensity (PI_{ZnO}) of ZnO is lowered by annealing, irrespective of the IGZO deposition method. With sputtering and without RTA, increasing the IR_{O2} value increased the carrier mobility (M_b), but decreased the resistivity (R) and carrier concentration (C_c), irrespective of the deposition power. After the RTA, carrier concentration and resistivity are lowered, and carrier mobility is risen. With e-beam evaporation and without RTA, the vague interface between Ti and IGZO films and the void defects in IGZO make these electrical properties more complicated in behavior and dependent on IGZO deposition time. Specimen's resistivity was lowered and carrier concentration was elevated by applying the RTA. The deposition of the Ti film as top layer can result in a much bigger reduction of R and further increases in M_b and C_c for these two IGZO deposition methods as compared to those shown in Ref. [1].

1. Introduction

The amorphous (a)-IGZO material is a promising transparent conducting oxide. It has been applied to attain a high performance

* Corresponding author. 1 University Road, Tainan City 701, Taiwan.
Tel.: +886 6 2757575x62155; fax: +886 6 2352973.
** Corresponding author. 1 University Road, Tainan City 701, Taiwan.
E-mail address: jflin@mail.ncku.edu.tw (J.-F. Lin).

https://doi.org/10.1016/j.jallcom.2018.07.252
0925-8388/

for thin film transistor (TFTs) [2–4], active-matrix liquid crystal displays [5], light-emitting diode displays [6], and LCD display applications [7]. Amorphous indium gallium zinc oxide (a-IGZO) TFTs have attracted much attention for applications in electronic and opto-electronic devices due to their relatively large field-effect mobility.

Several studies have examined the characteristics of a-IGZO films. The electrical properties and photosensitivity of a-IGZO degrade with increasing O content and decreasing density of electrons [8]. The addition of hydrogen and heat treatment have great impact on the carrier concentration and electrical resistivity of a-IGZO films [9]. The effects of O_2 plasma immersion on the electrical properties and transistor performance of IGZO films can be attributed to a reduction of oxygen-related defects in the films [10].

a-IGZO TFTs with a Ti/Cu source/drain were fabricated to reduce data-line resistance [11]. An indium-deficient IGZO layer was the origin of the reduction of the oxygen vacancy concentration in the channel. Specific contact resistances between a-IGZO and metallic electrodes (Ag, Au, In, Pt, Ti) were examined [12,13]. Low contact electrical resistances were obtained for Ag, In, and Ti electrodes [12]. The low-resistance Ti contact to a-IGZO can be ascribed to the effect of the structural relaxation of a-IGZO films at elevated temperatures and the interfacial reaction between Ti/Au and a-IGZO, which produced oxygen vacancies near the surface. A Ti contact with an a-IGZO channel also results in higher saturation mobility [14,15]. The performance of a TFT device with n-type Ti-doped GaZnO as the channel layer has verified that the crystal quality is improved and oxygen vacancies decreased when the O_2/Ar ratio increased [16].

In order to understand the effect of post-deposition thermal treatment, one study [17] presented the experimental results of sputter-deposited films after annealing. Thermal treatment can change the electron conduction properties [18]. Upon annealing at temperatures up to 500 °C for the preparation of a-IGZO films using the radio-frequency (RF) magnetron sputtering operation at room temperature, the optical band gap and number of oxygen vacancies increased, and the surface became smooth [19]. The electrical, optical, and structural properties of a-IGZO films were examined before and after annealing [20]. The carrier concentration and resistivity greatly depend on the addition of hydrogen and heat treatment. Lee et al. [21] examined the effects of composition on the electrical characteristics and optical properties of a-IGZO films. The average transmittance of a-IGZO films with more zinc atoms was greater than 80% because of the higher oxygen absorption of the zinc atoms [22]. Increase in oxygen vacancies of a-IGZO film could result in the increase in carrier concentration and reduction in resistivity [23]. In the review [24] focusing on the applications of new advanced energy electrode materials, microwave-assisted synthesis has been reported to be an efficient approach to control the composition and morphology of solids. In the study of Ur Rehman et al. [25], a new phase cubic π-SnSe was investigated under pressure. The lattice parameters and cell volume show an inverse relation to the pressure which might be the key factor for the enhancement of the near/mid infrared light activity. The thermoelectric properties of this material was explored [26]; and figure of merit was shown with the temperature rise; an insight for prospective applications in optoelectronics and clean energy storage devices had been studied [27].

Defects, including hillocks and nanovoids, are frequently found in bottom-gate TFTs due to stress migration arising at a high annealing temperature [28,29]. Hillocks form preferentially at grain boundaries or triple points due to fusion creep [30–32]. For all film compositions, the number of hillocks increases rapidly with temperature [33]. Nathan et al. [34] carried out a study on the effect of sputter deposition conditions on hillock formation. The threshold value of the annealing stress (σ_{an}) required for the formation of hillocks was determined [35]. The stress change parameter, $\sigma_f - \sigma_{an}$ (σ_f: internal stress after annealing), is a positive value that increases linearly with negative σ_{an}. The number of hillocks increases linearly with $(\sigma_f - \sigma_{an})$ when $(\sigma_f - \sigma_{an})$ is beyond the threshold.

Graphene has been studied extensively due to its unique characteristics. It has obtained a large potential applications in ultrasensitive strain tensor [36], organic photovoltaic cells and field effect transistors [37], bioimaging and related fields [38,39], high-speed electronics [40]. Allen et al. [40] gave a review to discuss the progresses in the production of graphene and its implementation in devices. In the study of Zhang et al. [37], applications of graphene formed by CVD, including as flexible transparent conductors for organic photovoltaic cells and field effect transistors were discussed. Monolayer graphene oxide was found to have a lower effective Young's modulus compared to that of pristine graphene [41]. Stone-Wales defects generally deteriorate sheet strength of graphene [42,43]. Graphene has the unique ability to reconstruct its lattice around intrinsic defects via the smart manipulations of defects, impurities, and adsorbates [44]. Impurities and adsorbates act as dopants to enhance carrier concentration, controlling n- and p-type conductions for transistor applications [45]. The effects of the graphene layer in an IGZO/graphene+Ni/SiO_2/Si wafer sample on optical and electrical properties show that the incorporation of the O atoms in IGZO into graphene as substitutional impurities resulted in a sharp drop in electrical resistance [46].

The study in Ref. [1] shows that a deposition of grapheme film in the IGZO/Ti/Graphene/polyimide specimens could enhance the crystallizations of IGZO (0012) significantly, and has brought in a big drop in the electrical resistivity, especially after applying a sufficiently high annealing temperature. These performances inspire us that the integrity sustenance of the graphene layer after the deposition of IGZO and the improvement of the Ti-induced crystallizations in the IGZO film are the key factors for the electrical properties of specimens. The present study focuses on the advantage of coating the Ti film as the top layer of specimen to improve the IR_{O2} of oxygen vacancies in the structure and the ability of preserving the graphene integrity after depositing the IGZO film by the two methods. RF magnetron sputtering and e-beam evaporation are two methods commonly applied to deposit IGZO films. Ion-beam irradiation becomes attractive due to its reliability, controllability, and noncontact deposition process. However, it shows drawbacks such as the effect by the composition of the deposited material and the high energy required to modify the surface of material [47]. The radio-frequency (RF) sputtering using the oblique deposition technique shows the advantage that the nanostructure can be fabricated on the substrate without the direct influence on the surface composition of the deposited materials, and the uniformity can be achieved by lowering the deposition power [7]. The differences in their deposition principle and conditions for the composite film and the protection of the graphene integrity after the IGZO deposition lead to big differences in the microstructures of the composite films and their interface, which cause significant effects on electrical, optical, and mechanical properties. The causes for these differences in properties are seldom studied. In the present study, Ti/IGZO/graphene/polyimide specimens were prepared, with the IGZO deposition conducted using RF magnetron sputtering (the S method) and e-beam evaporation (the E method), respectively. The Ti film was deposited as the top layer in order to investigate the IGZO crystallization effect on the electrical properties of the specimens before and after rapid thermal annealing (RTA). The two deposition methods produced the IGZO film either with different deposition power or different

deposition time. Eight kinds of specimen were thus prepared. RTA was applied to change the specimen microstructure and the void defects in the composite film. X-ray diffraction (XRD) was used to determine the mean diameter (D) of the TiO_2 (101) particles. The effect of D on three mean surface roughness parameters was also evaluated. The microstructures in the Ti, IGZO, and graphene layers and the interfaces of these layers created before and after RTA were investigated, and the distinction between the two IGZO deposition methods was identified. X-ray photoelectron spectroscopy (XPS) spectra of the Ti $2p_3$, O 1s, Zn $2p_3$, Ga 3d, and C 1s core levels and their deconvolutions were obtained. The deconvolutions of O 1s were used for the evaluation of the peak intensity ratio of oxygen vacancies (IR_{O2}). The effects of RTA and the IGZO deposition method on IR_{O2} and defects formed in microstructure were examined. The XPS peak intensities (PIs) of the oxides formed in the specimens and microstructure defects were presented to establish their correlations to the IR_{O2} change electrical properties, and band gap energy. From the comparisons of the results in the present study and Ref. [1], the superiorities of placing the Ti film as the top layer of specimen for the band gap energy (E_g) and the three electrical properties can be investigated.

2. Experimental details

Many studies have used a plastic substrate for flexible displays [48]. Polyimide was chosen as the substrate material in the present study, which was cleaned with acetone, isopropanol, and deionized (DI) water in sequence, with each cleaning process carried out in an ultrasonic cleaner for 10 min. Then, graphene, which was synthesized using chemical vapor deposition (CVD) over copper, was transferred onto the polyimide substrate. The percentage of the monolayer is over 95% when graphene is synthesized using CVD over copper [49].

The method of wet transfer was used for graphene production in this study since it can maintain the integrity of graphene film [50]. There are four steps in the transfer process: building a support, etching, transfer, and cleaning. A polymer, namely poly(methyl methacrylate) (PMMA), was first spin-coated onto the graphene. A thinner layer is more difficult to graphene transfer, but less of it remains. Then the PMMA/graphene/Cu specimen was heated at a stage to solidify the PMMA as the protection layer. Then, the Cu surface of the specimen was dipped in the $FeCl_3$ solution to remove the Cu foil. The DI water rinsed the PMMA/graphene several times to get rid of the Cu remains. The graphene/PMMA layer was then attached to the target substrate. Finally, the polymer protection layer was removed using an organic solution (acetone) and annealing. Applying PMMA as a support is necessary because without it, the graphene would be scattered after copper etching. The amount of PMMA was reduced by annealing but few PMMA still remained, as detected by atomic force microscopy and XPS. Nevertheless, the properties of graphene were acceptable from the conductivity tests.

After the graphene was transferred, two coating methods were used to prepare the IGZO film, namely sputter deposition and e-beam evaporation, respectively. Sputter deposition is a physical vapor deposition (PVD) method (defined as the S method) of thin film by sputtering. This involves ejecting material from a target that is a source onto a substrate. At sufficiently high gas pressures, the ions collide with the gas atoms which act as a moderator and move diffusively, reaching the substrates or vacuum chamber wall and condensing after undergoing a random walk. The entire range from high-energy ballistic impact to low-energy thermalized motion is accessible by changing the background gas pressure. Electron-beam evaporation (the E method) is also a method of physical vapor deposition in which a target anode is bombarded with an electron beam given off by a charged tungsten filament under high vacuums. The electron beam causes atoms from the target to transform into the gaseous phase. These atoms then precipitate into solid form, coating everything in the vacuum chamber with a thin layer of the anode material. For the S method, a mole ratio of In:Ga:Zn = 1:1:1 was used for the target. A pressure of 20 mTorr and an argon flow rate of 20 sccm were used. Sputtering was conducted at a deposition power of 60 and 100 W respectively for 30 min. The details of the sputtering conditions are shown in Table 1. According to the SEM image of specimen's lateral surface prepared using a focused ion beam (FIB), IGZO thicknesses of 46.2 and 102.0 nm were obtained for specimens synthesized at 60 and 100 W, which are coded as 60S and 100S, respectively. For the E method, IGZO film with thicknesses of 60.5 and 104.4 nm, coded as 60E and 100E respectively, were prepared by varying the deposition time. The base pressure was 2×10^{-5} Torr; the pressure became 6×10^{-5} Torr after the introduction of oxygen. The substrate was heated up to 200 °C during the deposition process. The deposition rate was around 0.8 Å/s. The evaporation conditions are detailed in Table 2. After the deposition of the IGZO film, a Ti film was deposited as the top layer with a deposition time of 15 min. The deposition conditions are shown in Table 3. The film thickness of the Ti film still varied with the deposition method of IGZO, even though the same deposition conditions for Ti were applied. Half of the specimens with each of the four codes were further treated using RTA. The annealing process was carried out under high-vacuum conditions (2×10^{-5} Torr) and at 300 °C for 1 h. The letter "R" marked behind either subscript "S" or "E" represents that a specimen had been annealed. The thickness data of Ti film before RTA are shown in Table 4. The precise thickness of the Ti film after the RTA are not provided because this film was forced to protrude upward by the micro voids formed in the IGZO + graphene layer and thus became zigzag profiles in large areas.

The thin films were examined using a JEOL 200 kV TEM. X-ray photoelectron spectroscopy (XPS) analyses were performed using a spectrometer (Physical Electronics, PHI 5000 VersaProbe) with monochromatic Al Kα (1486.6 eV) X-ray radiation. An X-ray diffraction (XRD, Bruker AXS Gmbh, Germany) was used for crystalline analyses. The wavelength λ of the XRD is 0.15405 nm.

3. Results and discussion

The morphology and the average surface roughness (Ra) of specimen before RTA are strongly dependent on the deposition method of IGZO. Fig. 1(a) shows the scanning electron microscopy (SEM) image of the 60S specimen; Fig. 1(b) shows the SEM image for the 60E specimen. Island-shaped bulges formed in the 60S specimens are distributed sparsely over the top surface with fine Ti grains, they will be identified to be due to the void defects generated in the IGZO layer including the interface of the IGZO + graphene layer and the polyimide substrate. For the 60E specimen, numerous Ti grains with a relatively larger mean size (about 50 nm) were uniformly and densely distributing over the surface without larger-size bulge. They make the mean surface roughness (Ra ≒ 7.7 nm) of specimen to be still smooth. The mean

Table 1
Details of sputtering (S) conditions.

Target	IGZO
Power (W)	60, 100
Chamber pressure (Torr)	20×10^{-3}
Substrate temperature	Room temperature
Sputtering time (s)	1800
Ar flow rate (sccm)	20

Table 2
Details of e-beam evaporation (E) conditions.

Target	IGZO
Power	4 kV × 30 mA
Deposition rate (Å/s)	0.8
Substrate temperature (°C)	200
Chamber pressure before introduction of oxygen (Torr)	2×10^{-5}
Chamber pressure after introduction of oxygen (Torr)	6×10^{-5}

Table 3
Details of Ti film deposition.

Target	Ti
Power	6 kV × 40 mA
Chamber pressure (Torr)	5×10^{-6}
Deposition rate (Å/s)	0.8
Substrate temperature	Room temperature
Thickness (nm)	80

surface roughness (Ra) data of these four specimens are shown in Table 4. They show the following characteristics: (1) the Ra values (17.0–23.0 nm) for the specimens prepared by sputtering are generally larger than those (14.6–17.0 nm) for the specimens prepared by e-beam evaporation; (2) a small difference in Ra exists between the specimens even if operating at different IGZO deposition power in the S method; (3) the Ra values of the specimens increase with increasing the deposition time in the E method. The measurements of Ra for the four specimens after RTA were also conducted. Fig. 2(a) shows the SEM image of the 60SR specimen. The quantity of budges after the RTA increases as compared with that shown in Fig. 1(a). As the lateral surface profiles shown in later section, these bulges were produced due to the formations of microvoids and defects. The number of bulges is determined by the annealing stress (σ_{an}) and the difference in the stress after finishing annealing (σ_f) and σ_{an}, it increases with increasing either (negative) σ_{an} or (σ_f - σ_{an}) [51] after the RTA. From the results obtained before and after RTA, the following behaviors can be drawn: (1) when the deposition power was at 60 W, the number of newly formed bulges increased after annealing; (2) when the deposition power was risen to 100 W, both the number and mean height of bulges after annealing increased. Fig. 2(b) shows the SEM image of the 60ER specimen. There is a little change in the number of grains between the code-E and -ER specimens. This feature is valid, for different deposition time in the E method. The Ra values in the 60SR, 100SR, 60ER, and 100ER specimens are relatively shown in Table 4. The changes in Ra due to the annealing for the 60SR and 100SR specimens are larger compared to those for the 60ER and 100ER specimens. Ra results indicate that the RTA use has increased surface roughness.

Specimen's average surface roughness is mainly governed by the quantity of bulges/grains formed on the specimen surface, and the mean grain (D) size of the crystalline microstructure. The bulges are related to the defects such as voids/cracks formed in the thin films. Fig. 3(a)-(d) show cross-section SEM images of the 60S, 100S, 60E, and 100E specimens, respectively. For the 60S and 60E specimens, the microstructure of all layers are quite solid and dense (see Fig. 3(a) and (c)). However, when the total thickness of the Ti and IGZO layers increased to be sufficiently large by increasing either the power or time, many voids and even microcracks formed in the IGZO layer (see Fig. 3(b) and (d)). These microstructural defects were produced beneath the bulges. The growth of defects (bulges/microvoids) perhaps occurred during the preparation of the IGZO+graphene and Ti layers. The size and amount of these defects are affected by RTA. The cross sections of the 100SR and 100ER specimens are shown in Fig. 4(a) and (b), respectively. Two comparisons, between Figs. 3(b) and 4(a) and between Figs. 3(d) and 4(b), show that the mean size and quantity of defects increase after RTA, irrespective of the deposition method of IGZO. According to the literature [35], the numbers of bulges and voids are proportional to the $\Delta\sigma$ ($= \sigma_f - \sigma_{an}$) values during film deposition. The $\Delta\sigma$ value generally increases with increasing temperature and thus deposition power. The defects in the code-S specimens prepared with different power and without RTA also satisfy this behavior. The explanations for the defects created in the code-E specimens prepared at the same deposition conditions but different deposition time, and thus different thickness, are made on the basis of the (negative) annealing stress, σ_{an}, formed in specimen during the annealing process. This stress was developed in the study of Flinn et al. [52] and expressed as

$$\sigma_{an} = B\{\ln(B/R) - \ln[t + (B/R)\cdot\exp(-\sigma_0/B)]\} \quad (1.a)$$

$$B = 5kT/lb \quad (1.b)$$

$$R = [E/(\ell - \upsilon)]\cdot\dot{\varepsilon}_0 \exp(-\Delta F/kT) \quad (1.c)$$

where k: Boltzmann's constant; T: the absolute temperature; λ: the absolute spacing ($= 10^2$b); υ: poisson's Ratio; b: Burgers vector; $\triangle F$: the total Helmholtz free energy required to surmount an obstacle in the absence of applied stress; $\dot{\varepsilon}_0$: the characteristic constant ($= 10^6$/s ~10^8/s); t: operating time; σ_0: specimen's stress before annealing; and E: elastic modulus.

The initial stress, σ_0, in Eq. (1.a) for a specimen is determined as

$$(\sigma_0) = \sqrt{(\sigma_0)_x^2 + (\sigma_0)_y^2} \quad (2.a)$$

where $(\sigma_0)_x$ and $(\sigma_0)_y$ are obtained using Stoney's formula:

Table 4
Mean surface roughness (R_a), film thicknesses of IGZO and Ti films, and mean diameter of TiO_2 (101) grains for Ti/IGZO/graphene/PI specimens.

Specimen code		Parameter			
		Average roughness (nm)	Film thickness (nm)		Diameter (D) of TiO_2 (101) particles (nm)
		Ra	IGZO	Ti	
(Code S)	60S	17.2	46.2	79.9	6.6
	60SR	19.1	–	–	7.0
	100S	17.0	102.0	83.7	7.1
	100SR	23.0	–	–	6.9
(Code E)	60E	7.7	60.5	61.1	6.2
	60ER	7.8	–	–	6.4
	100E	11.0	104.4	86.7	6.7
	100ER	14.6	–	–	6.3

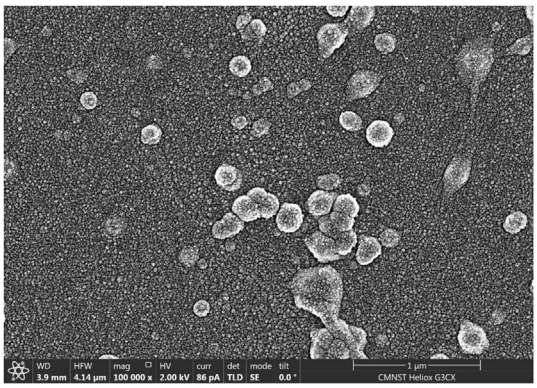

(a)

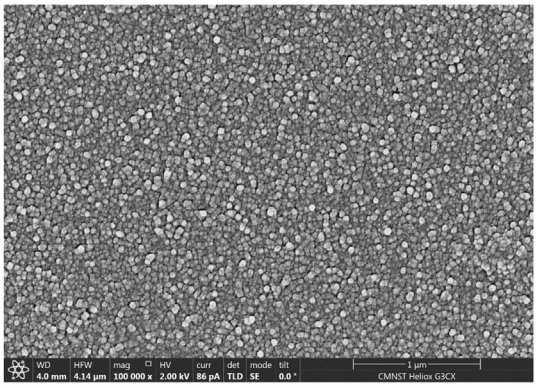

(b)

Fig. 1. SEM images of (a) 60S, and (b) 60E specimens before RTA.

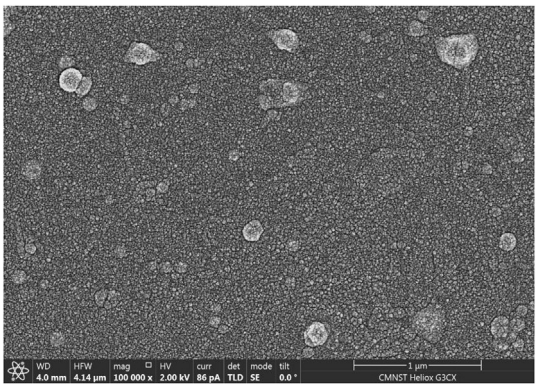

(a)

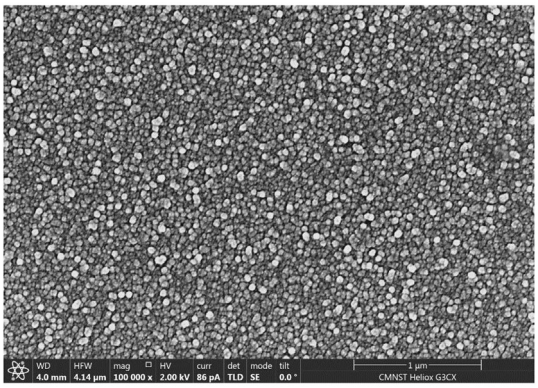

(b)

Fig. 2. SEM images of (a) 60SR, and (b) 60ER, specimens after RTA.

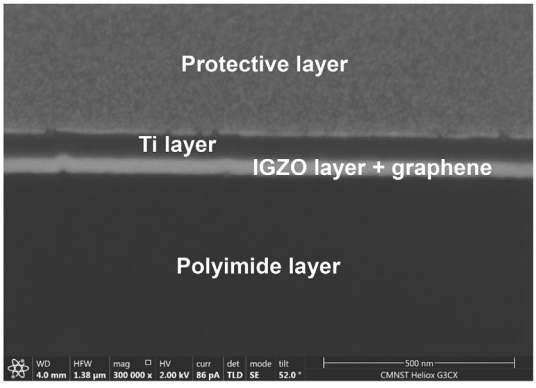

(a)

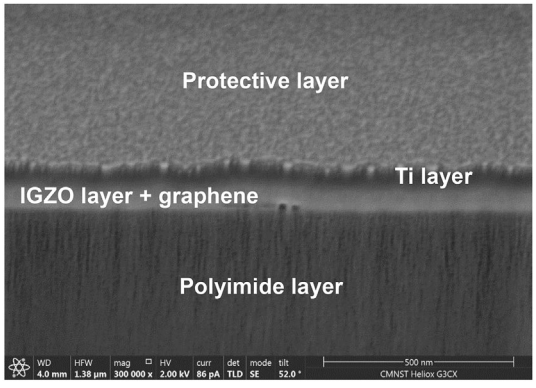

(c)

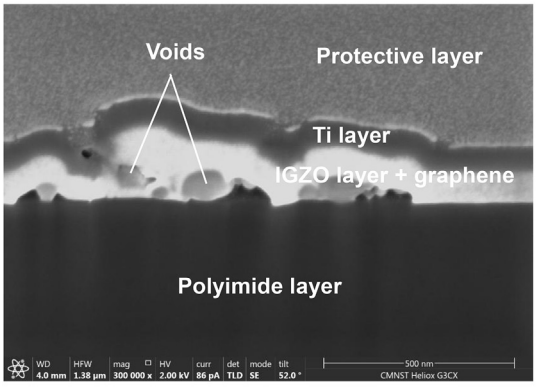

(b)

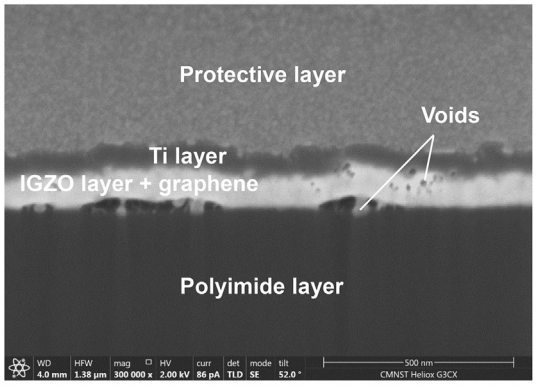

(d)

Fig. 3. SEM images of lateral surfaces of (a) 60S, (b) 100S, (c) 60E, and (d) 100E specimens before RTA.

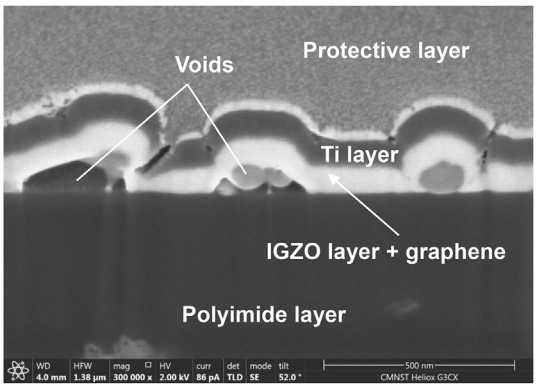

(a)

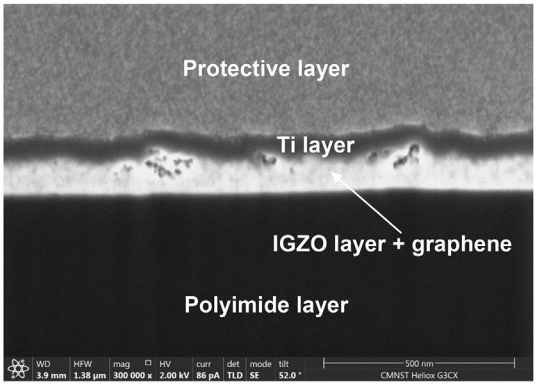

(b)

Fig. 4. SEM images of lateral surfaces of (a) 100SR and (b) 100ER specimens after RTA.

$$(\sigma_0)_{x/y} = \frac{1}{6}\frac{E_s d_2^s}{(1-\upsilon_s)d_f}\left(\frac{1}{(R)_{x/y}} - \frac{1}{(R_0)_{x/y}}\right) \quad (2.b)$$

where d_f, d_s: the thickness of film(s) and substrate, respectively; R, R_0: radii of curvature after and before the deposition of thin film(s), respectively; E_s: elastic modulus of substrate; υ_s: Poisson's ratio of the substrate. In the code-E specimens, increasing the deposition time and thus film thickness, d_f, according to Eq. (2.b), can reduce the (positive) value of σ_0. Then Eq. (1.a) shows that negative annealing stress, σ_{an}, increases with increasing the deposition time and decreasing σ_0. Define σ_f as the final stress after finishing the annealing. Then, the simulational results show that bulge defects increase with increasing the (positive) value of (σ_f - σ_{an}) too. The above illustration is provided to fit the behavior demonstrated in the code-E specimens without RTA.

The XRD patterns of the 60S, 60SR, 100S, and 100SR specimens are shown in Fig. 5 and those for the 60E, 60ER, 100E and 100ER specimens also have been made. The peaks at $2\theta \approx 26^\circ$ corresponding to the sole crystalline phase for all eight specimens are identified as TiO_2 (101) (anatase). The full width at half maximum (FWHM) values of these XRD patterns can be used to evaluate the grain size of TiO_2. The grain diameter (D) can be estimated from the Scherrer equation [53]. Table 4 shows the D values for the TiO_2 (101) crystals generated in these eight specimens. The results indicate that the D values for the code-S specimens (6.6–7.1 nm) are slightly larger than those (6.2–6.7 nm) for the code-E specimens. The trend in the D results due to the RTA is found to resemble that demonstrated in Ra. It is concluded that a relatively larger surface roughness of a specimen is partly attributable to TiO_2 (101) crystals with a relatively larger grain size. The D data in Table 4 also depend on the total thickness of the IGZO and Ti films. In these two categories of specimens, an application of RTA to a specimen with a relatively smaller total film thickness can increase the mean grain size of TiO_2.

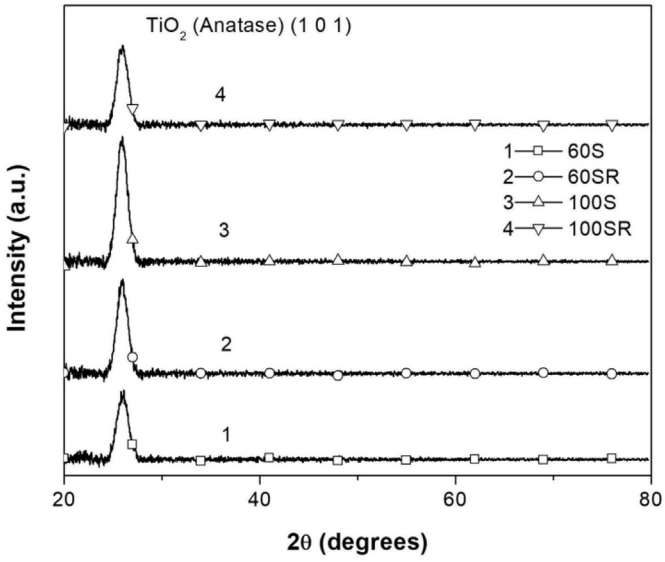

Fig. 5. XRD patterns of 60S, 60SR, 100S, and 100SR specimens.

A Raman system (Jobin Yvon/Labram HR-800UV, France) was utilized to inspect the graphene/polyimide specimen before depositing IGZO. In Fig. 6(a), the peaks at 1598 and 2690 cm^{-1} are identified as the G-band and 2D-band, respectively. The D-band peak at 1349 cm^{-1} is negligibly small. The 2D-to G-band peak intensity ratio ($I_{2D}/I_G \cong 8$) has a value much larger than 1. Therefore, the monolayer graphene before the IGZO deposition was obtained to be a high quality. In order to investigate the Raman spectra for the graphene film in the Ti/IGZO/graphene/PI specimens, a Raman spectrometer (MRI532S, Protrustech, Taiwan) with a power of 127 mW was applied to detect it from the side of the PI substrate. The graphene layer was exposed after the ablation of the PI substrate by the laser beam of the spectrometer. The Raman spectra for the 60S and 60SR specimens are shown in Fig. 6(b). The results show that the peak intensity of 2D band is lower than those of D and G bands as the IGZO and Ti films were deposited in sequence ($I_{2D}/I_G \cong 0.38$). Therefore, the use of RTA can bring in a significant reduction of I_{2D}/I_G. Fig. 6(c) shows the Raman spectra for the 100S and 100SR specimens. The vertical line is shown as the Raman shift of 2D band. As the laser power is elevated to 100W, the peak intensities of the 2D band for these two specimens are lowered to be nearly undetectable. An increase in the deposition power seems unfavorable for the intensity of the 2D-band in the Raman spectrum. The Raman spectra for the code-E and -ER specimens are not presented because of their I_{2D}/I_G magnitude to be negligibly small too.

The XPS spectra for all eight specimens were acquired, but only those of the 60S and 60E specimens are shown in Fig. 7(a) and (b), respectively. The elements and bonds for the main peaks are identified. The peak marked for O 1s and ZnO at a binding energy (BE) of about 530 eV is the highest of those for these two kinds of specimen. For the 60S specimen, the peak for Ti $2p_{3/2}$, TiO_2, and In with a BE about 460 eV shows the second place, and that for TiC with a BE about 385 eV is the third. For the 60E specimen, the peak for Zn $2p_{3/2}$ and ZnO with a BE about 530 eV becomes the second place, and that for Ti $2p_{3/2}$, TiO_2, and In is the third. XPS analyses were conducted for the elementals, In, Ga, Zn, Ti, and O, in these

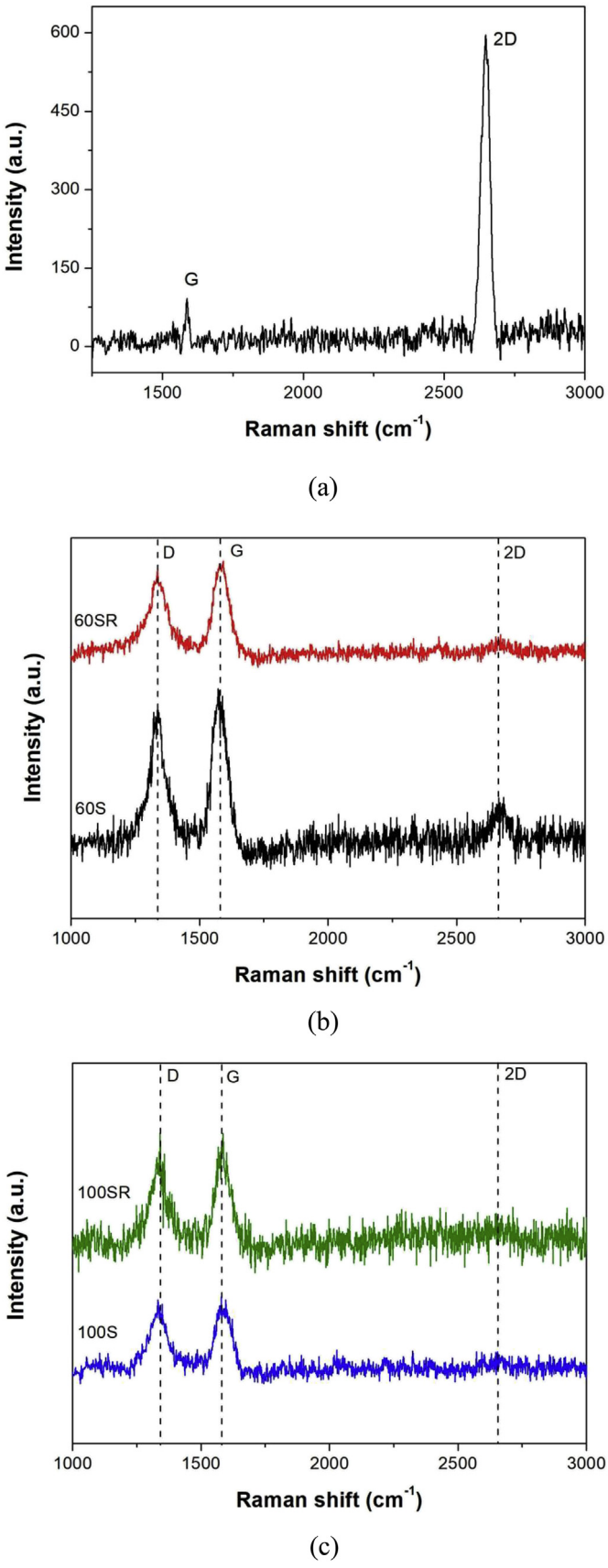

Fig. 6. Raman spectra for (a) the graphene/polyimide specimen; (b) the 60S and 60 SR specimens; and (c) the 100S and 100SR specimens.

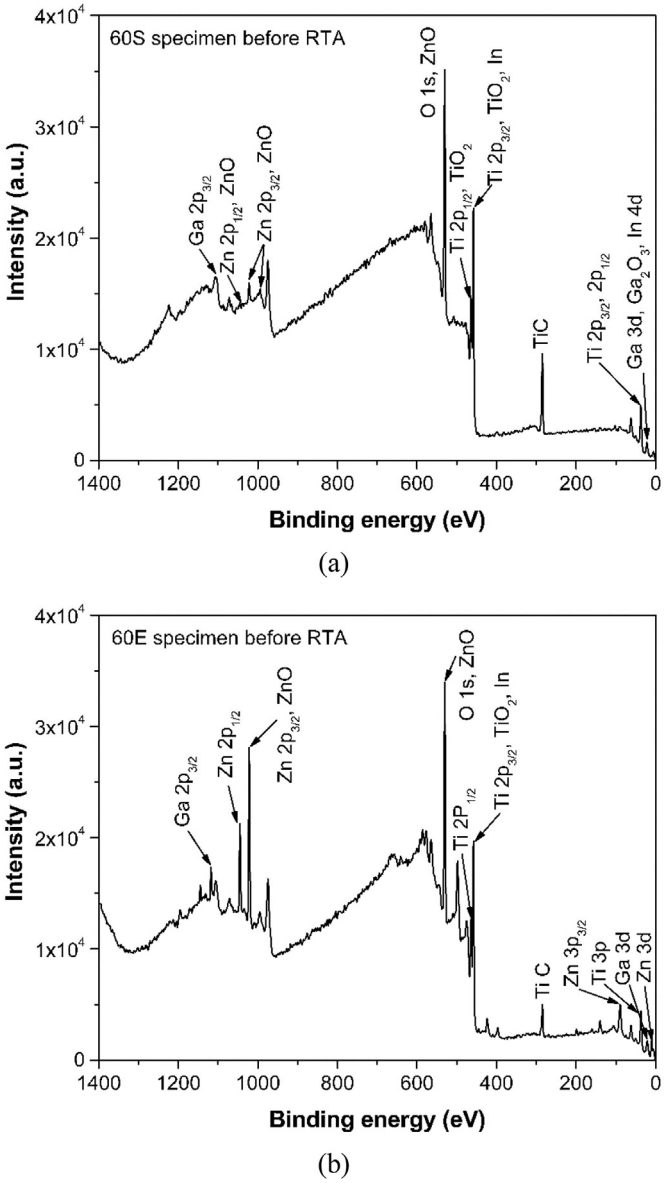

Fig. 7. The XPS spectra for the (a) 60S and (b) 60E specimens.

eight specimens. The XPS O 1s core level spectra for the 60S specimen are shown in Fig. 8 as the example. This spectrum can be further decomposed into three Gaussian-like spectra with BEs at about 530, 531, and 532 eV, respectively. The peak at ~530 eV (labeled as O1) is ascribed to the O^{2-} ions surrounded by metals In, Ga, and Zn atoms in the a-IGZO structure, representing oxygen in the oxide lattice without oxygen vacancies. The O2 peak (~531 eV) represents the oxygen vacancies or OH groups, which are produced with the oxygen-deficient regions. The O3 peak (~532 eV) corresponds to weakly bonded oxygen species on the film surface, and is attributable to H_2O and absorbed species integrated into the materials. Fig. 8 shows the decompositions of the O1s profiles for the 60S specimen. The peak intensities (PIs) of O1, O2, and O3 for the eight kinds of specimen are shown in Table 5. The peak intensity ratio (IR_{O2}) of O2 is defined as:

$$IR_{O2} = I_{O2}/(I_{O1} + I_{O2}) \quad (3)$$

The IR_{O2} values for the eight specimens are shown in Table 5. The

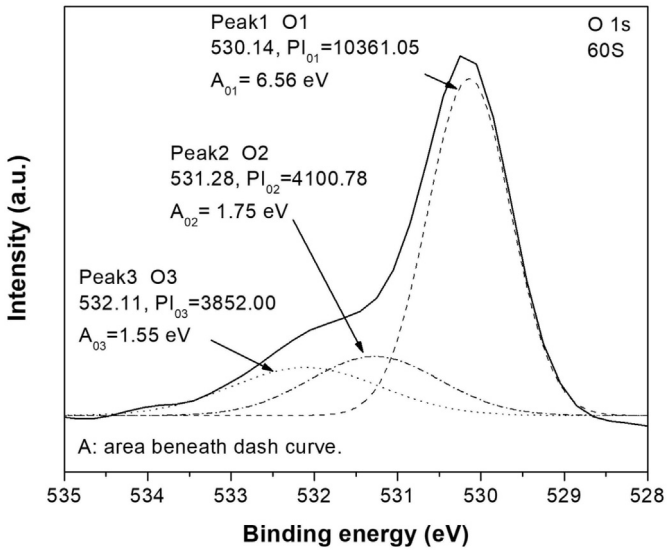

Fig. 8. Deconvolutions of O 1s XPS spectrum for the 60S and specimen.

effect of RTA on IR_{O2} for the code-S specimens is exactly opposite to that demonstrated for the code-E specimens. For the code-S specimens, the IR_{O2} values increase after RTA. Conversely, the IR_{O2} value decreases after applying RTA for the code-E specimens. In the specimens without RTA, an increase in either the deposition power or time had decreased IR_{O2}. The results of deconvolution area (DA) and full width half maximum (FWHM) for O1~O3 have been evaluated and shown in Table 5. However, the correlation among $(DA)_{O2}$ and $(FWHM)_{O2}$ and IR_{O2} due to the use of either the RTA or the deposition method of IGZO seems unable to establish.

An interesting correlation of IR_{O2} with peak intensities, PI_{TiO2} and PI_{Ti}, can be established; it depends on the annealing conditions and the deposition power/time. In the code-S and -E specimens before RTA, PI_{TiO2} is governed by the IR_{O2}. The results, $(PI_{TiO2})_{100S/E} > (PI_{TiO2})_{60S/E}$ and $(IR_{O2})_{60S/E} > (IR_{O2})_{100S/E}$, reveal that a decrease in PI_{TiO2} by decreasing either the deposition power or time had increased IR_{O2}. Subscript "S/E" is here defined as the property is valid for both the code-S and −E specimens. After the RTA, $(PI_{Ti})_{60S/E} > (PI_{Ti})_{60S/ER}$ and $(PI_{Ti})100_{S/ER} > (PI_{Ti})_{100S/E}$ exist; a decrease in PI_{Ti} always increased PI_{TiO2}, irrespective of the IGZO deposition method. With the S method and the RTA, an increase in IR_{O2} occurred for these two depositions powers. With the E method and the RTA, a decrease in IR_{O2} occurred for these two values of deposition time. IR_{O2} in a specimen has its magnitude affected by the TiO_2 intensity formed in the interfacial reactions between the IGZO and Ti layers and the defects created in the specimens. The details will be discussed in later section.

Fig. 9(a) and (b) show the XPS spectra of Zn 2p3 for the specimens prepared using the S and E methods, respectively. The BE

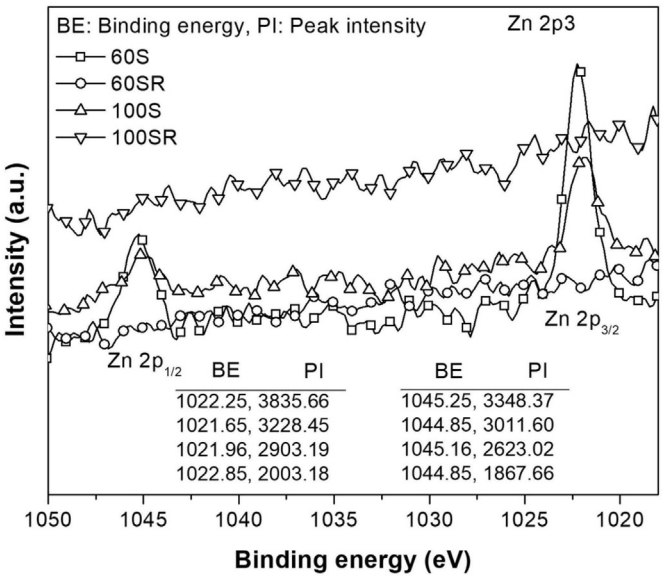

(a)

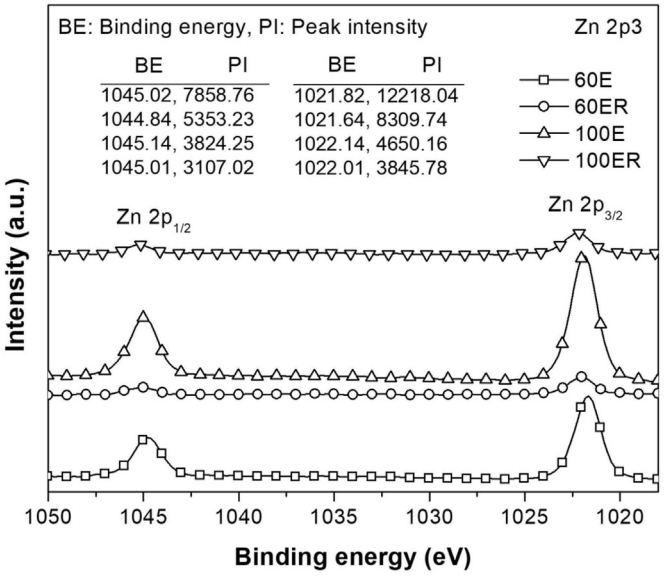

(b)

Fig. 9. Zn 2p3 XPS spectra for (a) 60S, 60SR, 100S, and 100SR specimens and (b) 60E, 60ER, 100E, and 100ER specimens.

Table 5
Peak intensities of O 1s and peak intensity ratios of eight kinds of specimen.

Specimen code		Peak intensities of O 1s (a.u.)			Deconvolution areas of O1s (eV)			FWHM (eV)			Peak intensity ratio $IR_{O2} = I_{O2}/(I_{O1}+I_{O2})$
		I_{O1}	I_{O2}	I_{O3}	O1	O2	O3	O1	O2	O3	
(Code S)	60S	10361.1	4100.8	3852.0	6.56	1.75	1.55	1.18	1.83	2.08	0.284
	60SR	7374.1	3687.1	4295.1	4.76	1.66	2.76	1.21	1.4	1.68	0.333
	100S	8806.3	3429.1	4812.8	5.30	0.48	3.07	1.16	0.76	1.87	0.280
	100SR	10362.9	5970.6	5126.7	6.44	3.16	2.89	1.15	1.34	1.68	0.366
(Code E)	60E	8100.3	4320.9	4663.0	4.56	1.30	3.24	1.10	0.96	2.04	0.348
	60ER	8762.3	3229.6	5424.5	5.88	0.89	3.65	1.23	1.37	1.58	0.269
	100E	11313.9	4505.3	4353.9	7.83	2.16	1.74	1.27	1.93	1.75	0.285
	100ER	11774.3	4486.9	5448.2	8.05	1.91	2.98	1.21	1.59	1.51	0.276

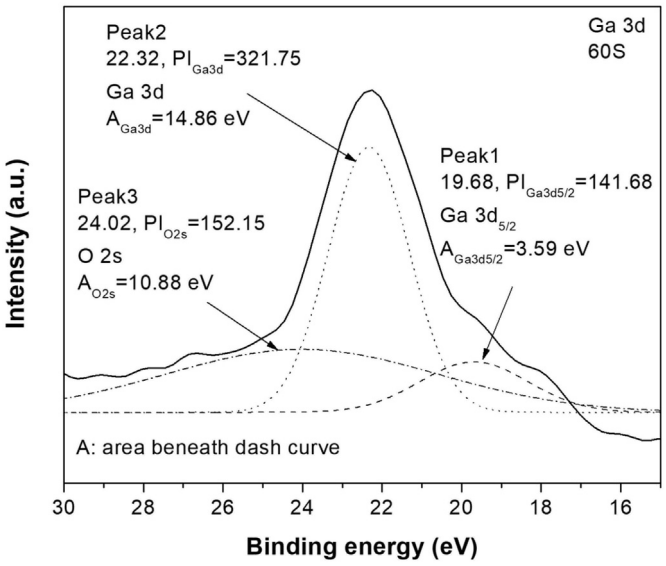

Fig. 10. Ga 3d XPS spectrum for the 60S specimens.

values corresponding to these two peaks are at about 1022 and 1045 eV, respectively. Each of these two peaks can be further deconvoluted into $Zn_{2p3/2}$, $Zn_{2p1/2}$ atoms (donor defects) and Zn-O band actually. The results are summarized as: (1) the peak intensities (PIs) of $Zn_{2p3/2}$ and $Zn_{2p1/2}$ in the specimens after RTA are lower than those before RTA, irrespective of the IGZO deposition method; (2) the specimens prepared by differing the deposition power/time show the results that $(PI_{Zn2p})_{60S} > (PI_{Zn2p})_{100S}$ and $(PI_{Zn2p})_{100E} > (PI_{Zn2p})_{60E}$ exist before RTA. The decrease in the atomic percentage of Zn_{2p} is partly due to zinc vacancy formation via the out-diffusion of Zn from the IGZO film [54]. Zinc vacancies created in the IGZO film deposited by sputtering are stronger than those formed by e-beam evaporation. The final outcome of these zinc vacancies is detailed in the later section.

Fig. 10 shows the XPS spectrum of Ga 3d for the 60S specimen as the example. This broad spectrum can be decomposed into three Gaussian spectra with BEs of about 20, 22, and 23.5 eV, to be identified as the Ga $3d_{5/2}$, Ga 3d atoms (donor defects), and O 2s (Ga–O) bond/atom, respectively [55,56]. The following values of PI values, the FWHM of intensity profile, and the area (DA) beneath the Gaussian intensity curve are evaluated for these eight specimens and shown in Table 6. The behaviors demonstrated in these three peak intensities of Ga 3d due to the RTA are found characteristically consistent with those shown in the deconvolution area, respectively; which are valid for both the code-S and -E specimens. The PI results are summarized and shown in Table 7. The same tendency is exhibited in the PIs of Ga $3d_{5/2}$ and Ga 3d after the RTA, irrespective of the IGZO deposition method. $PI_{Ga3d5/2}$ and PI_{Ga3d} are risen by applying the annealing to the code-S specimens; conversely, these two peak intensities are lowered by annealing the code-E specimens.

Fig. 11(a) and (b) show the C 1s spectra for the specimens whose IGZO film was prepared using sputtering and e-beam evaporation, respectively. The relatively higher peaks of these curves are investigated to be varying in a range of 284.75 eV–284.85 eV. The binding energy is slightly greater than the C=C species (sp^2 bonded carbon 284.5 eV) [57], but is smaller than the C-C species (adventitious carbon with an ubiquitous nonuniform carbonaceous layer, 285 eV) [57,58]. These peaks are thus formed to have the mixture of C=C and C-C species. Graphene is generally a one-atom thick covalently boned sp^2 carbon prototype 2D material. The binding energy results indicate that the graphene layer in the specimens has been partly turned out to be the impurities of adventitious carbon during the deposition of the IGZO onto the graphene surface. The lower peaks in these curves are varying in a range of 288.56 eV–288.75 eV, and their binding energy is lying between O-C=O (carbonyl carbon, 288 eV) [57] and COOH (carboxylic, 290.0 eV) [59]. Therefore, these peaks are created to be the mixture of these two species with O-C=O as the dominant one. The O-C=O bond created point defects in the graphite-like film during the deposition of the IGZO film, and then, substitutional impurities were produced at the interface of the IGZO and graphene layers. The RTA application to the same specimen yields $(PI_{O\text{-}C=O+COOH})_{S/E} > (PI_{O\text{-}C=O+COOH})_{S/ER}$, $(PI_{Adv.C+C=C})_S > (PI_{Adv.C+C=C})_{SR}$, and $(PI_{Adv.C+C=C})_{ER} > (PI_{Adv.C+C=C})_E$, irrespective of the IGZO deposition method. The results in Table 7 for the specimens without RTA show the characteristic that $PI_{Adv.C+C=C}$ decreases with increasing the $PI_{O\text{-}C=O+COOH}$, it is valid for these two deposition methods. The $PI_{Adv.C+C=C}$ is lowered by applying the RTA in the code-S specimens, whereas it is elevated in the code-E specimens. The effect of $PI_{Adv.C+C=C}$ on the band gap energy (E_g) will be examined later.

Fig. 12(a) and (b) show the Ti 2p3 spectra for the specimens whose IGZO film was prepared using sputtering and e-beam evaporation, respectively. In each XPS spectrum, there are two peaks, Ti $2p_{3/2}$ and Ti $2p_{1/2}$, with BEs of about 459 and 464.5 eV, respectively. The effects of RTA and the deposition method of IGZO on the PIs of these two kinds of Ti quantum number are summarized in Table 7. $(PI_{Ti2P})_{60S/E} > (PI_{Ti2P})_{60S/ER}$ and $(PI_{Ti2P})_{100S/ER} > (PI_{Ti2P})_{100S/E}$ are obtained in response to the RTA use; and $(PI_{Ti2P})_{60S} > (PI_{Ti2P})_{100S}$ and $(PI_{Ti2P})_{100E} > (PI_{Ti2P})_{60E}$ are obtained to respond the deposition method of IGZO. For a specimen without RTA, decreases in these two kinds of Ti peak intensity have increased the mean grain size (D) of TiO_2 in the code-S specimens and decreased the D value in the code-E specimen. The above characteristic is also valid for both the code-S and E specimens after the RTA. In this study, the I_{O2} parameter related to oxygen vacancies is also affected by the contacts of Ti with a-IGZO. Before RTA, increasing the PI of Ti 2p3 had increased (decreased) the IR_{O2} of

Table 6
Peak intensities, deconvolution areas, and full width half maximum values of Ga3d.

Specimen code	Peak intensities of Ga3d			Deconvolution areas of Ga3d (eV)			Full width half max. FWHM (eV)		
	$Ga3d_{5/2}$	Ga3d	O2s	$Ga3d_{5/2}$	Ga3d	O2s	$Ga3d_{5/2}$	Ga3d	O2s
60S	141.68	321.75	152.15	3.59	14.86	10.88	3.21	2.41	8.01
60SR	103.52	173.58	201.82	1.84	6.06	17.40	3.96	2.48	5.62
100S	138.40	270.55	154.64	5.45	11.17	8.85	6.24	2.39	6.28
100SR	145.63	366.26	190.12	1.20	18.33	16.03	1.25	2.55	7.43
60E	264.05	324.14	182.76	6.39	13.61	7.70	1.70	2.48	5.10
60ER	188.66	280.02	201.17	4.34	8.49	10.08	2.70	2.04	5.20
100E	341.59	363.46	197.64	11.36	23.56	8.53	2.06	2.23	6.58
100ER	179.11	353.18	212.89	1.22	20.23	16.36	0.83	3.15	6.64

Table 7
Comparisons for the intensities of Ti 2p3, O 1s, Zn 2p3, Ga3d, and C 1s, and diameter of TiO_2 particles for the code-S and -E specimens before and after RTA.

Specimen condition	Deposition method of IGZO	Ti 2p3	O 1s	Zn 2p3	Ga 3d		C 1s		Mean size of TiO_2 particles, D (nm)
		Ti $2p_{3/2}$, Ti $2p_{1/2}$	IR_{O2}	Zn $2p_{3/2}$, Zn $2p_{1/2}$	Ga $3d_{5/2}$	O 2s	C-C (Adventitious C) + C-C	O+C=O + COOH	
RTA effect	Sputtering (S)	$(PI)_{60S/E} > (PI)_{60S/ER}$	$(IR_{O2})_{SR} > (IR_{O2})_S$	$(PI)_{S/E} > (PI)_{S/ER}$ valid for two deposition methods with different deposition power/time	$(PI)_{SR} > (PI)_S$	$(PI)_{S/ER} > (PI)_{S/E}$ valid for two deposition methods with different deposition power/time	$(PI)_S > (PI)_{SR}$	$(PI)_{S/E} > (PI)_{S/ER}$ valid for two deposition methods with different deposition power/time	$(D)_{60S/ER} > (D)_{60S/E}$
	E-beam evaporation (E)	$(PI)_{100S/ER} > (PI)_{100S/E}$	$(IR_{O2})_E > (IR_{O2})_{ER}$		$(PI)_E > (PI)_{ER}$		$(PI)_{ER} > (PI)_E$		$(D)_{100S/E} > (D)_{100S/ER}$
Effect of increasing the deposition power or time (without RTA)	Sputtering (S)	$(PI)_{60S} > (PI)_{100S}$	$(IR_{O2})_{60S/E} > (IR_{O2})_{100S/E}$	$(PI)_{60S} > (PI)_{100S}$	$(PI)_{60S} > (PI)_{100S}$	$(PI)_{100S} > (PI)_{60S}$	$(PI)_{60S} > (PI)_{100S}$	$(PI)_{60S} > (PI)_{100S}$	$(D)_{100S/E} > (D)_{60S/E}$
	E-beam evaporation (E)	$(PI)_{100E} > (PI)_{60E}$		$(PI)_{100E} > (PI)_{60E}$	$(PI)_{100E} > (PI)_{60E}$		$(PI)_{60E} > (PI)_{100E}$	$(PI)_{100E} > (PI)_{60E}$	

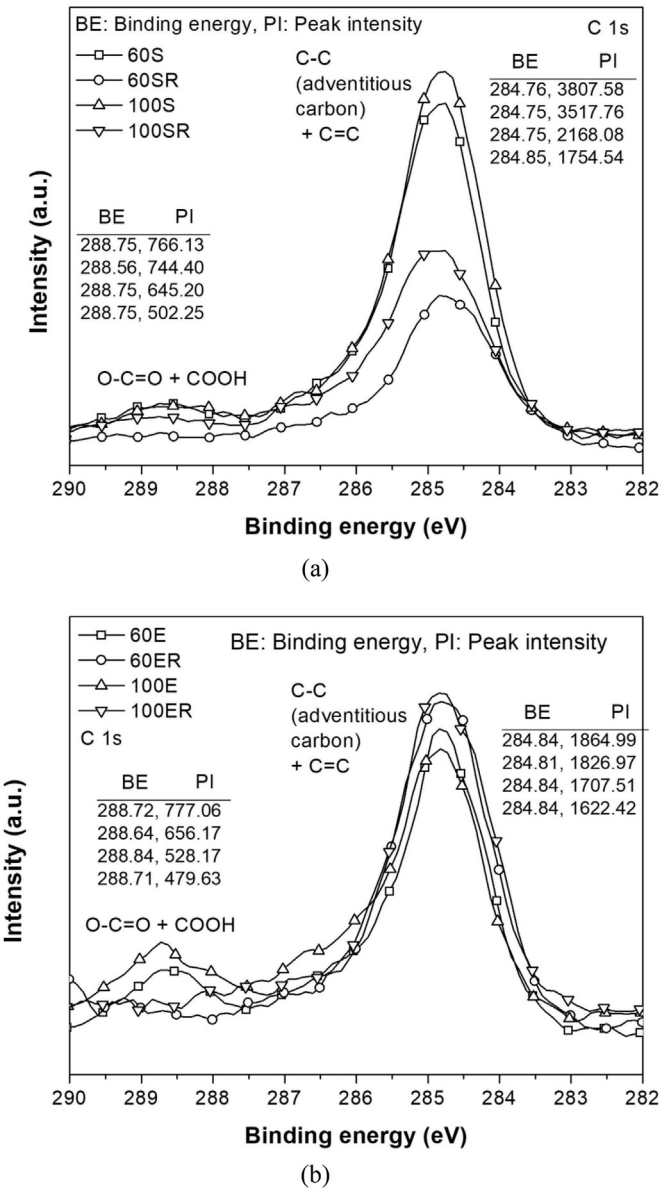

Fig. 11. C 1s XPS spectra for (a) 60S, 60SR, 100S, and 100SR specimens and (b) 60E, 60ER, 100E, and 100ER specimens.

specimen having their IGZO deposition with the sputtering (the e-beam evaporation) method. The connections among IR_{O2}, PI_{TiO2} and thus the electrical properties are discussed later.

The results in Table 7 allow us to summarize as follows: (1) In the code-S specimens after the RTA, IR_{O2} and PI_{O2S} increased and $PI_{Adv.C+C=C}$, $PI_{O-C=O+COOH}$ and PI_{Zn2P} decreased; the other PI values, however, depended on the deposition power. (2) For the IGZO deposition using the E method, the application of RTA reduced IR_{O2}, $PI_{Ga3d5/2}$, PI_{Ga3d}, and $PI_{O-C=O+COOH}$ but raised PI_{Zn2p}, PI_{O2S} and $PI_{Adv.C+C=C}$; (3) In the code-S specimens without RTA, increasing the deposition power of IGZO has decreased the values of IR_{O2}, PI_{Ti2p3}, PI_{Zn2p}, $PI_{Ga3d5/2}$, PI_{Ga3d} and $PI_{O-C=O+COOH}$, but increased PI_{O2s} and $PI_{Adv.C+C=C}$; (4) In the code-E specimens without RTA, increasing the deposition time of IGZO has brought in decreases in IR_{O2} and $PI_{Adv.C+C=C}$, but the increases in PI_{Ti2p3}, PI_{Zn2p3}, $PI_{Ga3d5/2}$, PI_{Ga3d}, PI_{O2s} and $PI_{O-C=O+COOH}$. The above results reveal the characteristic that the PI values for Ti_{2p3}, Ga_{3d} (except for O_{2s}) and C1s produced in the code-S specimens without RTA demonstrate their

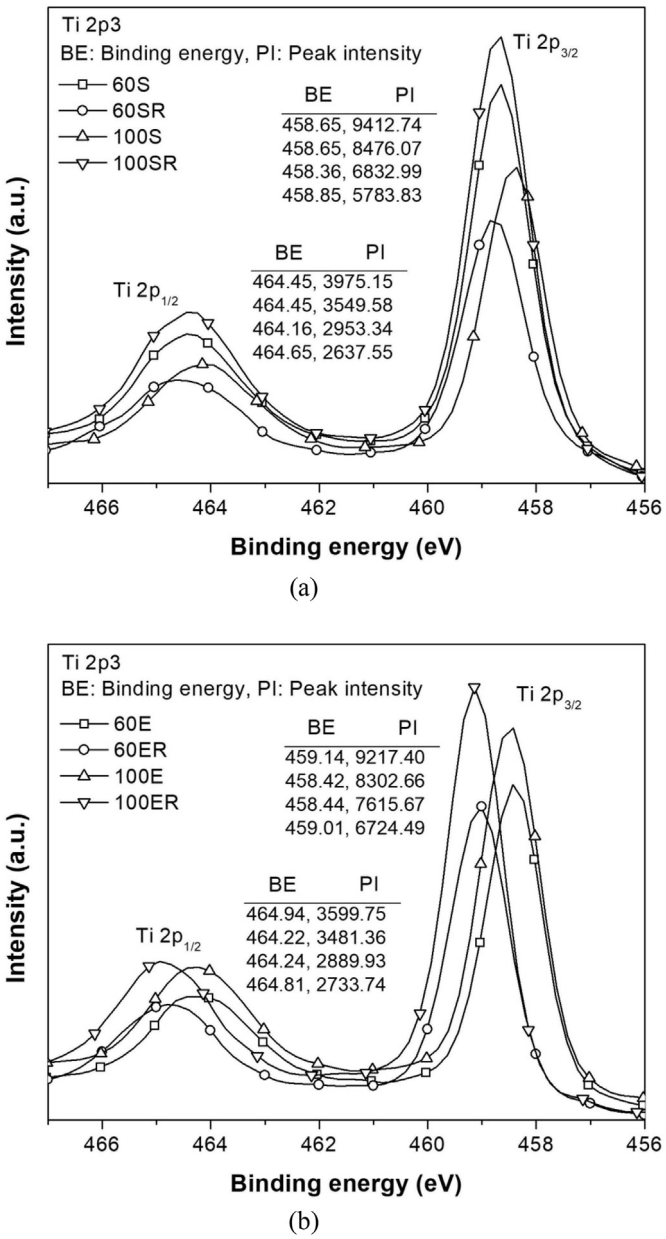

Fig. 12. Ti 2p3 XPS spectra for (a) 60S, 60SR, 100S, and 100SR specimens and (b) 60E, 60ER, 100E, and 100ER specimens.

behavior basically opposite to that exhibited in the code-E specimens. This can be ascribed to the difference in the structure the integrity of graphene film and the defects in the microstructure after depositing the IGZO and Ti films by these two methods.

The determinations of the binding energy for the oxides were carried out by referring to the NIST X-ray Photoelectron Spectroscopy Database. Fig. 13(a)-(c) show the XPS spectra for the oxides of TiO_2, ZnO, and Ga_2O_3 respectively, which are created in the 60S, 60SR, 60E, and 60ER specimens. The BEs for the peaks at about 464.5 and 458.7 eV are identified as TiO_2. The XPS spectra of ZnO are distributed with the peaks at ~530 eV and ~1022 and 1045 eV, respectively. The peak intensity data in Tables 7 and 8 reveal that a decrease in the PI_{Ti2p3} can result in an increase in the PI_{TiO2} of specimen for these two IGZO deposition methods. For the oxide of Ga_2O_3, Ga is one of the known elements in the host composite film. It contains seven possible spectral lines which include $2p_{3/2}$, 3d, $3d_{3/2}$, $3d_{5/2}$, $3p_{1/2}$, $3p_{3/2}$ and 3s and demonstrate the energy between 20.0 and 22.5 eV. The PI results of these oxides are obtained in order to examine the RTA effect on the PI of oxides. Table 8 shows the changes of PI for these three oxides in the specimens before and after the RTA. The IR_{O2} comparisons are also made in order to investigate the correlations of IR_{O2} with PI_{TiO2}, PI_{ZnO}, and PI_{Ga2O3}: (1) with the S method, an increase in PI_{TiO2} by the RTA results in an increase in IR_{O2} and decreases in PI_{ZnO} (~530 eV) and PI_{Ga2O3} for the 60S and 60SR specimens; conversely, a decrease in PI_{TiO2} and increases in PI_{ZnO}(~530 eV) and PI_{Ga2O3} for the 100S and 100SR specimens; (2) with the E method, a decrease in PI_{TiO2} created in the specimens without RTA results in an increase in IR_{O2} and increases in PI_{ZnO} (~530 eV) and PI_{Ga2O3} for the 60E and 60ER specimens; conversely, an increase in PI_{TiO2} and decreases in PI_{ZnO} (~530 eV) and PI_{Ga2O3} for the 100E and 100ER specimens; (3) the application of RTA results in the reduction of PI_{ZnO}, irrespective of the two IGZO deposition methods; (4) increasing PI_{TiO2} can decrease PI_{ZnO} (~530 eV) and PI_{Ga2O3}, irrespective of the deposition method of IGZO.

The study of Choi and Kim [14] shows that an increase in the intensity of TiO_2 formed in the interfacial reaction between Ti and the a-IGZO layer is favorable for the rise of IR_{O2}, which can bring in the chemical reduction of oxygen ions and release of electrons simultaneously, thus resulting in the elevation of carrier mobility. However, this behavior is valid for the applications of RTA to the 60S and 60E specimens only. That is, the effect of RTA on the PI_{TiO2} and IR_{O2} of these two kinds of specimen demonstrates its behavior consistent with that of the study [14]. It is found that the validity of this correlation between PI_{TiO2} and IR_{O2} exists only in the specimens without forming noticeable microvoids in the IGZO layer. The opposite behavior is exhibited in the 100S and 100E specimens, it can be ascribed to the microvoid defects shown in the microstructure, irrespective of the RTA use.

Fig. 14(a) shows a SEM image of the lateral surface of the 60S specimen without bulge (hillock). “1”, “2”, “3”, and “4” are marked for the positions of the Ti film, the interface between Ti and IGZO films, the IGZO film, and the interface between IGZO+graphene and the polyimide substrate, respectively. In Fig. 14(b), the crystalline areas with d-spacing were identified, by referring the International Centre for Diffraction Data (ICDD) files, as TiO_2 (101, 111) particles formed during the Ti deposition. The oxygen ions decomposed from IGZO have reacted with titanium under vacuum conditions (5×10^{-5} Torr). The matrix materials prepared by the E method are identified to be amorphous Ti film. The selected area electron diffraction (SAED) pattern of the transmission electron microscopy (TEM) reveals that TiO_2 (101), (110), (111), and (002) coexisted, and that (101) was dominant. Fig. 14(c) shows the microstructure near the interface between the Ti and IGZO films. On the IGZO side of the interface, labeled as "2" in Fig. 14(a), the microstructure is amorphous. For region "3", within the IGZO film, the TEM image and SAED pattern (not shown here) also confirm that the film is amorphous. Fig. 14(d) shows the TEM image of the area marked as "4", which includes the graphene film lying between the IGZO film and the polyimide substrate. The graphene film (thickness: 2–3 nm) shows an intact layer still existing after the sequential depositions of the IGZO and Ti films.

Fig. 15(a) shows the lateral surface of the 60SR specimen in a position without bulge. “1” to “4” are the positions near those shown in Fig. 14(a). Fig. 15(b) shows the TEM image of the Ti film marked by “1”. The crystalline materials were identified with the aid of ICDD files. The pitch values measured on the crystal plane for these areas are shown in the first column of the table below this figure. The pitch values of the crystals of Ti (100), Ti (101), Ti (102), and TiO_2 (101) are shown in the second column. The crystals and orientations corresponding to these areas are shown in the third

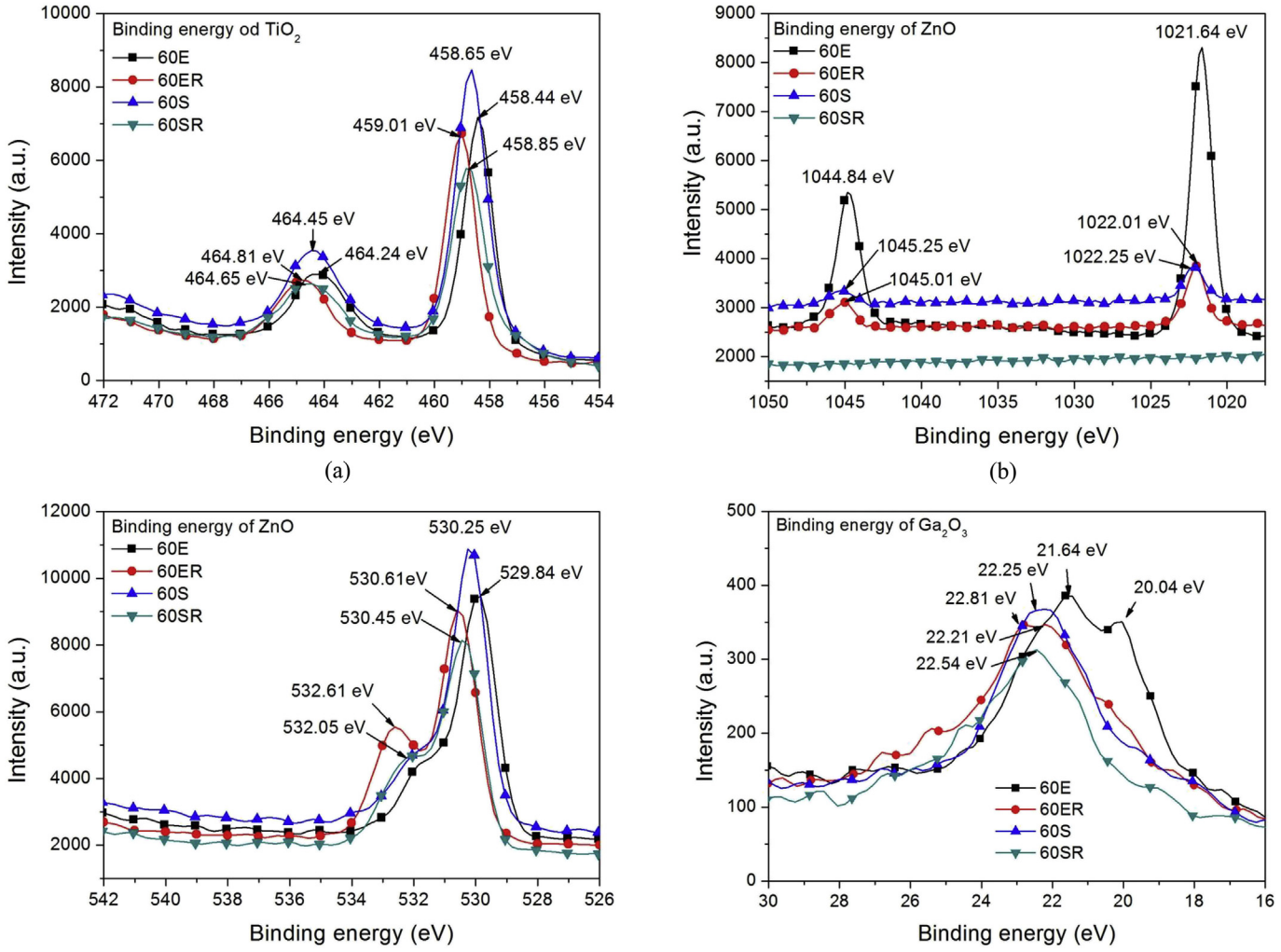

Fig. 13. XPS spectrum for (a) TiO_2, (b) ZnO, and (c) Ga_2O_3 oxides.

Table 8
Comparisons for the results of IR_{O2}, PI_{TiO2}, PI_{ZnO}, and PI_{Ga2O3} in code-S and -E specimens before and after RTA.

Deposition method of IGZO	Specimen code	IR_{O2}	PI_{TiO2}	PI_{ZnO}		PI_{Ga2O3}
				BE: ~530 eV	BE: ~1022 eV and 1045 eV	
Sputtering method	60S 100S	$(IR_{O2})_{SR} > (IR_{O2})_S$, irrespective of the deposition power of IGZO	$(PI_{TiO2})_{60SR} > (PI_{TiO2})_{60S}$ $(PI_{TiO2})_{100S} > (PI_{TiO2})_{100SR}$	$(PI_{ZnO})_{60S} > (PI_{ZnO})_{60SR}$ $(PI_{ZnO})_{100SR} > (PI_{ZnO})_{100S}$	$(PI_{ZnO})_S > (PI_{ZnO})_{SR}$	$(PI_{Ga2O3})_{60S} > (PI_{Ga2O3})_{60SR}$ $(PI_{Ga2O3})_{100SR} > (PI_{Ga2O3})_{100S}$
E-beam evaporation method	60E 100E	$(IR_{O2})_E > (IR_{O2})_{ER}$, irrespective of the deposition time of IGZO	$(PI_{TiO2})_{60ER} > (PI_{TiO2})_{60E}$ $(PI_{TiO2})_{100E} > (PI_{TiO2})_{100ER}$	$(PI_{ZnO})_{60E} > (PI_{ZnO})_{60ER}$ $(PI_{ZnO})_{100ER} > (PI_{ZnO})_{100E}$	$(PI_{ZnO})_E > (PI_{ZnO})_{ER}$	$(PI_{Ga2O3})_{60E} > (PI_{Ga2O3})_{60ER}$ $(PI_{Ga2O3})_{100ER} > (PI_{Ga2O3})_{100E}$

column. The Ti layer of the 60SR specimen is thus composed of a-Ti, Ti (100), Ti (101), Ti (102), and TiO_2 (101). A TEM image of an area including the Ti-IGZO interface is shown in Fig. 15(c). The boundary of the Ti and IGZO films can be identified clearly via the difference in darkness. In the IGZO layer nearby the interface, the three crystalline areas marked by 0.322, 0.213, and 0.245 nm are identified as TiO_2 (101), Ti (101), and Ti (100), respectively. Of note, they are a flat head in the interface and exist on the IGZO side only. In the deposition of the Ti film, TiO_2 particles where formed in this layer, they can cause oxygen vacancies in the IGZO film. These vacancies were refilled with Ti material via diffusion. In the RTA process, titanium was partly operating at a sufficiently high annealing temperature to react with the surrounding oxygen ions in the IGZO film to produce TiO_2 particles. This behavior explains why the TiO_2 particles formed on the IGZO side as well as with a flat head aligned with the interface.

Fig. 16(a) shows a SEM image of the lateral surface of the 60E specimen. There are two microstructures that are quite distinct from those shown in the 60S specimen. The first distinction is the interface of the Ti and IGZO films, which is presented to be a vague boundary; the second is the microstructure of the IGZO film full of void defects. The identification of defects will be discussed in a later section. The areas in Fig. 16(a) enclosed by dashed curves are identified to have TiO_2 (002) and (211) particles. A TEM image of the small area marked for the interface between Ti and IGZO films is shown in Fig. 16(b). In this figure, the boundary between the Ti and

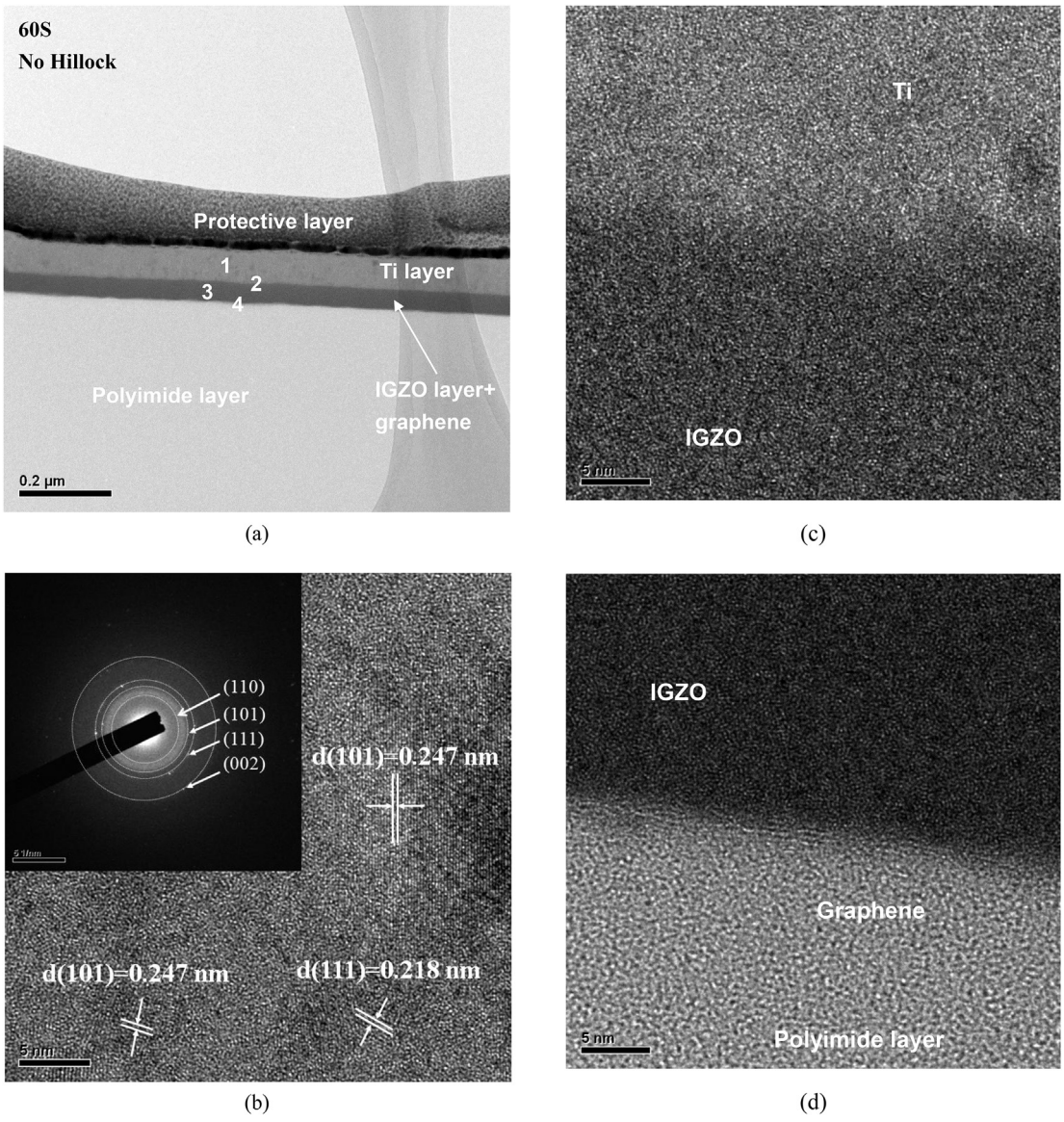

Fig. 14. (a) SEM micrograph of lateral surface of 60S specimen; (b) TEM image and SAED pattern of Ti layer; (c) TEM image of interface between Ti and IGZO layers; (d) TEM image of interface between IGZO+graphene and polyimide substrate.

IGZO films is indistinct. Additionally, there exists a relatively light area near the interface, but it seems more apt to be on the IGZO side. This area is identified as a void defect, which was formed during the deposition of IGZO using the E method. Here, the TEM image of the area within the IGZO film is not provided, but it is full of void defects whose pattern resembles that shown in the light areas of Fig. 16(b). Fig. 16(c) shows the microstructures of the areas of IGZO, graphene, and polyimide substrate. In the use of the E method, the graphene layer broke into disconnected, and was mixed with IGZO and voids during the deposition of IGZO. The thickness of the mixing region is much larger than that in the 60S specimen.

Fig. 17(a) shows a SEM image of the lateral surface of the 100ER specimen in the area without hillock. The horizontal white line indicates the energy-dispersive X-ray spectroscopy (EDX) scanning from the polyimide substrate to the protective layer of platinum. Fig. 17(b) shows the EDX spectra of the chemical elements, O, Ga, and Zn, in sequence. From the contrasts among these chemical elements, the depth regions in the spectra associated with the Ti and IGZO+graphene films and polyimide substrate are thus identified roughly. In the IGZO+graphene region in Fig. 17(a) for element O, white stains (void defects) on the right half of this region are quantitatively much more than those on the left half. The cps values for the chemical elements, Ga, Zn, and O, show a trend exactly opposite to that of the density of white stains shown in Fig. 17(a). That is, cps decreases in Ga, Zn, and O elements in the IGZO films due to the increase of voids in the microstructure result in the density increase of white stains.

Hall measurements were made to determine the carrier mobility (M_b), carrier concentration (C_c), and resistivity (R) of specimens. The data are shown in Table 9. The differences in the microstructure and defects between the two IGZO deposition methods have the carrier concentrations of the code-E and -ER specimens generally lower than those of the code-S and −SR specimens. However, the resistivities and carrier mobilities of the code-E and -ER specimens are higher than those of the code-S and -SR specimens.

The IR_{O2} value of specimen is obviously a controlling factor of

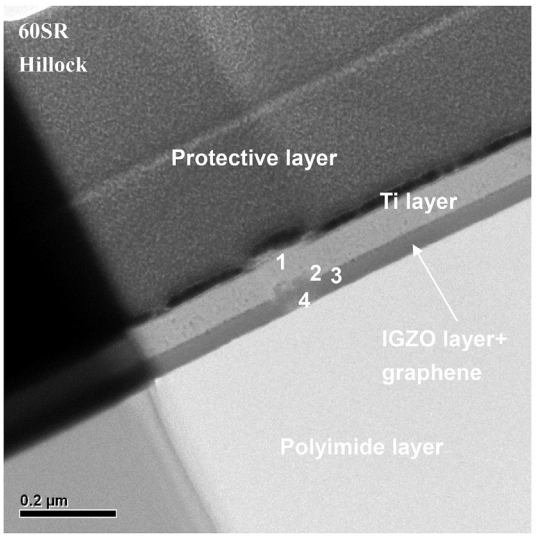

(a)

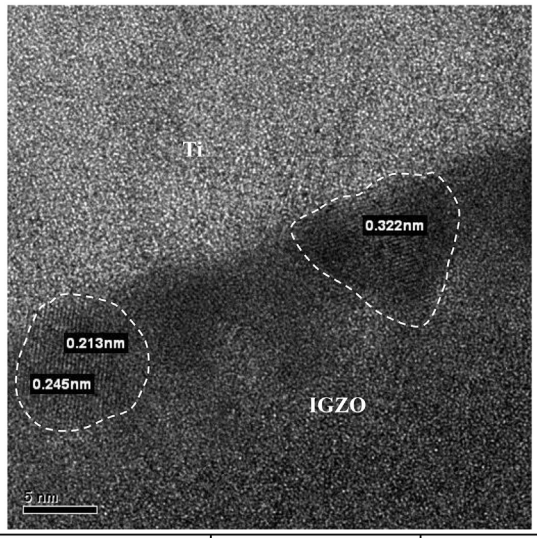

Measure value for pitch on crystal plane (nm)	Contrast between pitch and crystal orientation	Crystal orientation
0.322	TiO_2 (1 0 1) = 0.352	TiO_2 (1 0 1)
0.213	Ti (1 0 1) = 0.224	Ti (1 0 1)
0.245	Ti (1 0 0) = 0.256	Ti (1 0 0)

(c)

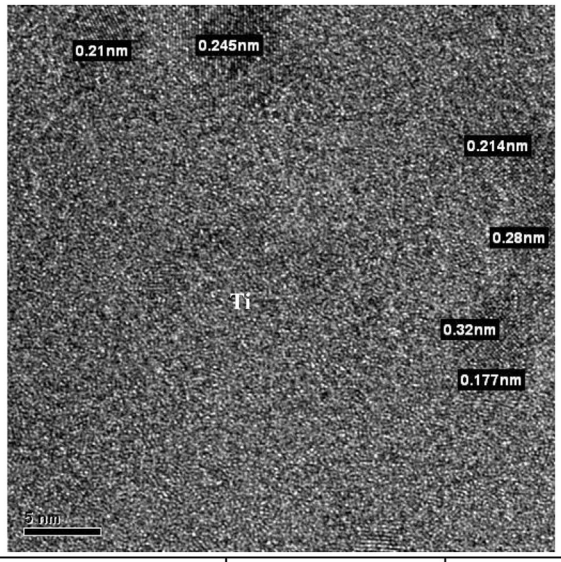

Measure value for pitch on the crystal plane (nm)	Contrast between pitch and crystal orientation	Crystal orientation
0.210	Ti (1 0 1) = 0.224	Ti (1 0 1)
0.245	Ti (1 0 0) = 0.256	Ti (1 0 0)
0.214	Ti (1 0 1) = 0.224	Ti (1 0 1)
0.280	Ti (1 0 0) = 0.256	Ti (1 0 0)
0.320	TiO_2 (1 0 1) = 0.352	TiO_2 (1 0 1)
0.177	Ti (1 0 2) = 0.173	Ti (1 0 2)

(b)

Fig. 15. (a) SEM micrograph of 60SR specimen; (b) TEM image of Ti layer; (c) TEM image of interface between Ti and IGZO layers.

electrical properties. With Ti as the source/drain electrode in the specimens, the interfacial reaction between Ti and a-IGZO is helpful for the generation of oxygen vacancies near the interface. An increase in oxygen vacancies is advantageous for the electron releases from the reduction of oxygen ions, thus resulting in an elevation of carrier mobility [14]. An increase in either deposition power or time can reduce specimen's IR_{O2}. Due to the distinctions in the microstructure integrity of graphene and the IGZO-Ti reaction between these two IGZO deposition methods, the IR_{O2} reduction in the code-S specimens without RTA can bring in an increase in C_c and decreases in R and M_b; conversely lead to a decrease in C_c and increases in R and M_b in the code-E specimens. As the RTA was applied, the IR_{O2} in the code-S specimens was elevated, and caused decreases in C_c and R and an increase in M_b; however, IR_{O2} was

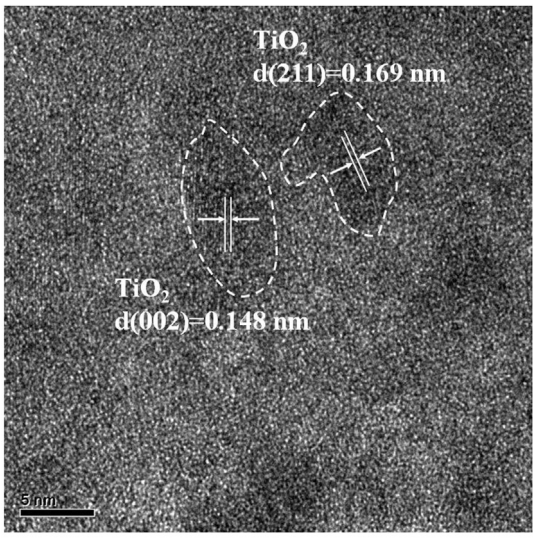

(a)

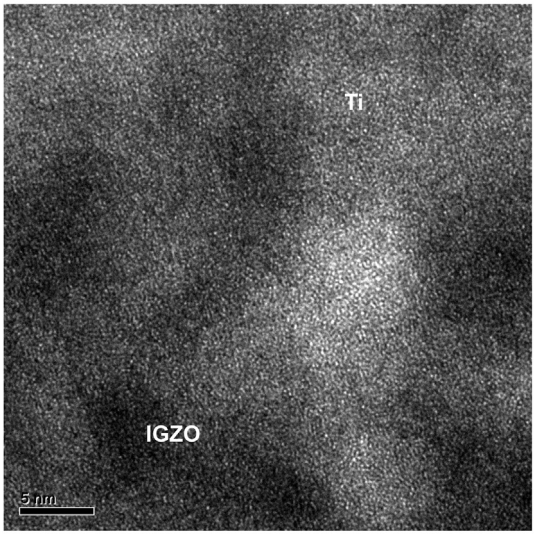

(b)

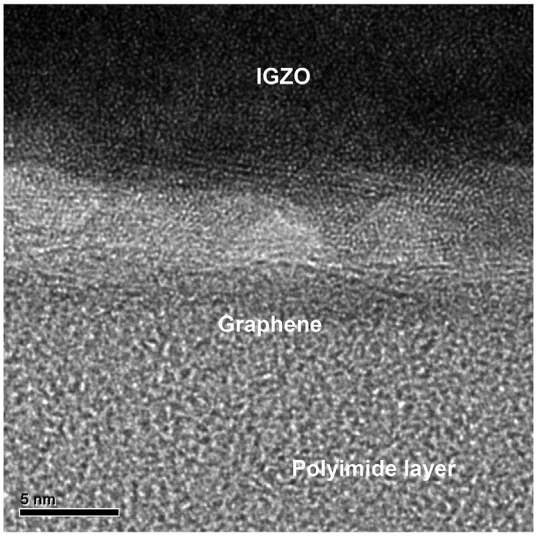

(c)

Fig. 16. (a) SEM micrograph of 60E specimen; (b) TEM image of interface between Ti and IGZO layers; (c) TEM image of interface between IGZO+graphene layer and polyimide substrate.

lowered in the code-E specimens, and caused an increase in C_c and a decrease in R. The behavior of M_b is, however, dependent upon the deposition time of IGZO. The specimens with the Ti film as the top layer have the electrical properties to compare with those shown in Ref. [1], where the Ti film was deposited below the IGZO film as the interlayer of IGZO and graphene. In the study of Ref. [1], 1.53 to 0.16 Ω cm and 1.13×10^{18} to 2.31×10^{17} cm^{-3} and 35.24 to 18.21 cm^2/V.S were obtained as the resistivity, carrier concentration and mobility, respectively. The resistivities created in this study (in a range of 1.003×10^{-2} to 5.541×10^{-3} Ω cm) are much lower and the carrier concentrations (in a range of 1.500×10^{20} to 1.300×10^{19} cm^{-3}) are much higher than those shown in Ref. [1].

The electrical resistivity of a-IGZO has been reported to be greatly affected by Ti contacts. In the present study of having the Ti film as the top layer, the results of the code-S specimens reveal that IR_{O2}, the diameter (D) and peak intensity (PI_{TiO2}) of TiO_2, and the mean size and quantity (SQD) of void defects have increased after applying the RTA, irrespective of the IGZO deposition method. However, the resistivity (R) is a parameter governed by the combined result of the above factors (disadvantageous for R reductions) and the IR_{O2}, which finally resulted in the R values in this study much lower than those in Ref. [1]. In the present study, a relatively lower electrical resistance obtained from increasing the Ti contacts is valid only for the conditions of $(PI_{Ti})_{100S/ER} > (PI_{Ti})_{100S/E}$ and $(PI_{Ti})_{60S} > (PI_{Ti})_{100S}$.

The data in Table 9 for these two IGZO deposition methods reveal that the maintenance of the graphene integrity and quality is of importance to have a relatively lower resistivity and carrier mobility and higher carrier concentration although the IR_{O2} value and the quantity and size of microvoids are also involved in the specimens after annealing.

The optical absorption coefficient (α) can be evaluated as [60]:

$$\alpha = \ln(1/T)\Big/t_f \tag{4}$$

if the transmission T and composite film thickness t_f are available. The optical energy (band) gap, E_g, can be evaluated as [61]:

$$(\alpha h_v)^2 = A(h_v - E_g) \tag{5}$$

where A is a constant, and h_v is the energy of photon. E_g can be determined by extrapolating the linear portion of the α^2-curve to intersect the h_v axis.

Table 9 shows the E_g values of the eight specimens prepared using sputtering and e-beam evaporation, respectively. $(E_g = 2.240\ eV)_{60SR} < (E_g = 2.247\ eV)_{60S}$ and $(E_g = 2.334\ eV)_{100SR} < (E_g = 2.402\ eV)_{100S}$, are shown in the code-S specimens, and $(E_g = 2.371\ eV)_{60E} < (E_g = 2.404\ eV)_{60ER}$ and $(E_g = 2.456\ eV)_{100E} < (E_g = 2.489\ eV)_{100ER}$, are the results in the code-E specimens. In the code-S specimens, the application of RTA can reduce the E_g, irrespective of the deposition power of IGZO. Conversely, the RTA can increase the E_g of the code-E specimens. The E_g value can be evaluated by increasing the deposition power in the code-S specimens or the deposition time in the code-E specimens. In general, graphene has its E_g to be very small. A specimen with a better graphene integrity and less voids in the structure and generally helpful to have a lower E_g. The above characteristic fits the E_g behavior demonstrated in the specimens with different IGZO deposition method. The results in Table 5, Table 7, and Table 9 show that E_g decreases with decreasing the $PI_{Adv.C+C=C}$ but increasing the IR_{O2}; this behavior is valid for both the two deposition methods of IGZO. Decreasing the E_g of specimen can decrease its carrier concentration. This behavior happens in the current n-type IGZO material because the electrons induced by oxygen vacancies

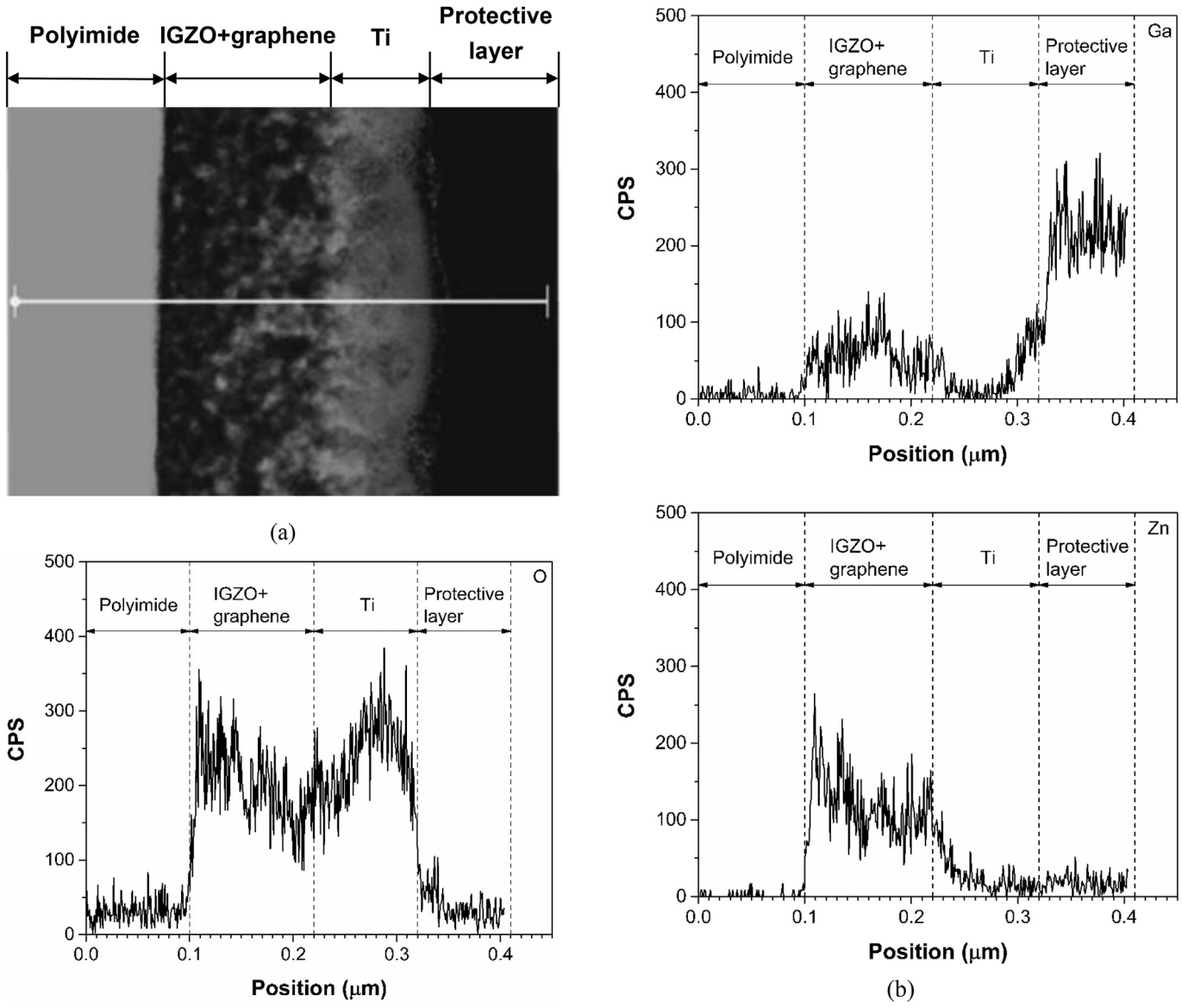

Fig. 17. (a) SEM image showing EDX scanning line for 100ER specimen; (b) EDX analyses for O, Ga, and Zn elements along scanning line across polyimide substrate, IGZO+graphene layer, Ti layer, and protective layer (PT).

Table 9
Results of mobility, resistivity, and carrier concentration and band gap energy for the eight specimens.

Specimen code	Mobility, Mb ($cm^2/V{\cdot}s$)	Resistivity, R ($\Omega{\cdot}cm$)	Carrier concentration, Cc (cm^{-3})	Band gap energy, E_g (eV)
60S	21.734	1.003×10^{-2}	2.866×10^{19}	2.247
60SR	88.192	5.451×10^{-3}	1.300×10^{19}	2.240
100S	6.207	6.715×10^{-3}	1.500×10^{20}	2.402
100SR	22.135	6.098×10^{-3}	4.630×10^{19}	2.334
60E	5.667×10^{2}	3.372×10^{-2}	3.271×10^{17}	2.371
60ER	7.798×10^{2}	6.977×10^{-3}	1.149×10^{18}	2.404
100E	5.933×10^{2}	7.760×10^{-2}	1.357×10^{17}	2.456
100ER	3.733×10^{2}	2.921×10^{-2}	5.733×10^{17}	2.489

accumulated in the conduction band such that the Fermi level lays in conduction band and the "apparent" band gap obtained from the experimental results is greater than the intrinsic band gap of IGZO with a difference indicating the Burstein-Moss shift. Due to the defect distinctions in the microstructure and the interface of the Ti and IGZO+graphene films, the resistivity behavior demonstrated in the code-S specimens after the RTA is consistent with the variation of E_g; however, its behavior in the code-E specimens is exactly opposite to that of E_g.

The results without annealing in Fig. 11(a) and (b) also show that the $(PI)_{C\text{-}C+C=C}$ value created in the sputtering method is higher than that by the e-beam evaporation method. This feature is

consistence with the results of the 2-D-band peak intensity shown in Fig. 6(b) and (c). Since the $(PI)_{C\text{-}C+C=C}$ parameter is an indication of graphene intensity, $((PI)_{C\text{-}C+C=C})_S > ((PI)_{C\text{-}C+C=C})_E$ has resulted in $(E_g)_E > (E_g)_S$, $(R)_E > (R)_S$, $(M_b)_E \gg (M_b)_S$, and $(C_c)_S > (C_c)_E$, irrespective of the IGZO deposition method.

4. Conclusion

Big differences in thin films' microstructure and the interface of Ti and IGZO+graphene topography are created in the specimens prepared by different deposition method of the IGZO film and the deposition conditions, they are the main causes of having distinctions in the electrical and mechanical properties. The mean surface roughness (R_a) of specimens whose IGZO film was produced by sputtering was generally larger than that of specimens whose IGZO film was prepared using e-beam evaporation. The RTA application increased the mean surface roughnesses of all specimens. Specimen's Ra is mainly governed by the formation of bulges in the specimen and the mean grain sizes of the oxides in the crystalline microstructures. The mean TiO_2 grain size and the quantity of bulges and microvoid defects increased after RTA, irrespective of the deposition method of IGZO.

The effect of RTA on IR_{O2} for the specimens whose IGZO film was prepared using sputtering is exactly opposite to that for the specimens prepared by the e-beam evaporation. For the specimens prepared using sputtering (e-beam evaporation), IR_{O2} increased (decreased) after RTA. For all specimens without RTA, an increase in either the deposition power or deposition time of the IGZO film can decrease IR_{O2}.

The interfacial reaction between Ti and a-IGZO becomes the dominant factor for the production of oxygen vacancies and thus the IR_{O2}. In the code-S specimens, the RTA use can elevate the IR_{O2}. However, the use of RTA can reduce the IR_{O2} in the code-E specimens. A rise of IR_{O2} can result in a rise of carrier mobility. A decrease in E_g can decrease the carrier mobility in the n-type IGZO film. In these two IGZO deposition methods, E_g decreases with deceasing the $PI_{Adv.C+C=C}$ relevant to the quality of graphene film in the specimen. The three electrical properties are determined to be the combined effect of the factors including IR_{O2}, E_g, the grain diameter (D) and peak intensity of TiO_2, and the mean size and quantity of void defects. An increase in the IR_{O2} of the code-S and −SR specimens results in the reductions of band gap energy (E_g), resistivity (R), and carrier concentration (C_c) but the rise of carrier mobility. An increase in the IR_{O2} of the code-E and −ER specimens brings in the rise of R and decreases in the E_g and C_c.

The better preservation of the graphene structure in the code-S and -SR specimens allows the resistivity and carrier mobility to be relatively lower, and the carrier concentration to be relatively higher compared to those shown in the code-E and −ER specimens.

The placement of a Ti film as the top layer can bring in much bigger drops in electrical resistivity and larger increases in carrier mobility and concentration compared to those created in the specimens with the Ti film placed below the IGZO layer. These features are valid for these two IGZO deposition methods.

References

[1] T.C. Li, C.F. Han, K.C. Hsieh, J.F. Lin, Effects of thin titanium and graphene depositions and annealing temperature on electrical, optical, and mechanical properties of IGZO/Ti/graphene/PI specimen, Ceram. Int. 44 (2018) 6573–6583.

[2] K. Song, D. Kim, X.S. Li, T. Jun, Y. Jeong, J. Moon, Solution processed invisible all-oxide thin film transistors, J. Mater. Chem. 19 (2009) 8881–8886.

[3] K. Nomura, H. Ohta, A. Takagi, T. Kamiya, M. Hirano, H. Hosono, Room-temperature fabrication of transparent flexible thin-film transistors using amorphous oxide semiconductors, Nature 432 (2004) 488–492.

[4] A. Sato, K. Abe, R. Hayashi, H. Kumomi, K. Nomura, T. Kamiya, M. Hirano, H. Hosono, Amorphous In–Ga–Zn–O coplanar homojunction thin-film transistor, Appl. Phys. Lett. 94 (2009), 133502 (3 pages).

[5] H.H. Hsieh, H.H. Lu, H.C. Ting, C.S. Chuang, C.Y. Chen, Y. Lin, Development of IGZO TFTs and their applications to next-generation flat-panel displays, J. Inf. Display 11 (2010) 160–164.

[6] J.B. Choi, Y.J. Chang, C.H. Park, B.R. Choi, H.S. Kim, K.C. Park, TFT backplane technologies for AMLCD and AMOLED applications, J. Kor. Phys. Soc. 54 (2009) 549–553.

[7] G.M. Wu, C.Y. Liu, A.K. Sahoo, RF sputtering deposited a-IGZO films for LCD alignment layer application, Appl. Surf. Sci. 354 (2015) 48–54.

[8] J. Yao, N. Xu, S. Deng, J. Chen, J. She, H.D. Shieh, P.T. Liu, Y.P. Huang, Electrical and photosensitive characteristics of a-IGZO TFTs related to oxygen vacancy, IEEE Trans. Electron. Dev. 58 (2011) 1121–1126.

[9] C.H. Jung, H.I. Kang, D.H. Yoon, The electrical, optical, and structural properties of amorphous indium gallium zinc oxide films and channel thin-film transistors, Solid State Electron. 79 (2013) 125–129.

[10] P. Liu, T.P. Chen, Z. Liu, C.S. Tan, K.C. Leong, Effect of O_2 plasma immersion on electrical properties and transistor performance of indium gallium zinc oxide thin films, Thin Solid Films 545 (2013) 533–536.

[11] Y.W. Lee, S.J. Kim, S.Y. Lee, W.G. Lee, K.S. Yoon, J.W. Park, J.Y. Kwon, M.K. Han, Effect of Ti/Cu source/drain on an amorphous IGZO TFT employing SiN_x passivation for low data-line resistance, Electrochem. Solid State Lett. 15 (2012) H126–H129.

[12] Y. Shimura, K. Nomura, H. Yanagi, T. Kamiya, M. Hirano, H. Hosono, Specific contact resistances between amorphous oxide semiconductor In–Ga–Zn–O and metallic electrodes, Thin Solid Films 516 (2008) 5899–5902.

[13] H. Kim, K.K. Kim, S.N. Lee, J.H. Ryou, R.D. Dupuis, Low resistance Ti/Au contacts to amorphous gallium indium zinc oxides, Appl. Phys. Lett. 98 (2011), 112107 (3 pages).

[14] K.H. Choi, H.K. Kim, Correlation between Ti source/drain contact and performance of InGaZnO-based thin film transistors, Appl. Phys. Lett. 102 (5) (2013), 052103.

[15] H.H. Hsu, C.Y. Chang, C.H. Cheng, S.H. Chiou, C.H. Huang, High mobility bilayer metal–oxide thin film transistors using titanium-doped InGaZnO, IEEE Electron. Device Lett. 35 (2014) 87–89.

[16] W.S. Liu, Y.M. Wang, Enhancing transparent thin-film transistor device performances by using a Ti-doped GaZnO channel layer, RSC Adv. 5 (2015) 104392–104399.

[17] H. Yabuta, N. Kaji, M. Shimada, T. Aiba, K. Takada, H. Omura, T. Mukaide, I. Hirosawa, T. Koganezawa, H. Kumomi, Microscopic structure and electrical transport property of sputter-deposited amorphous indium-gallium-zinc oxide semiconductor films, in: The 26th Symposium on Plasma Sciences for Materials, vol. 518, 2014, 012001 (27 pages).

[18] H. Yabuta, M. Sano, K. Abe, T. Aiba, T. Den, H. Kumomi, High-mobility thin-film transistor with amorphous $InGaZnO_4$ channel fabricated by room temperature rf-magnetron sputtering, Appl. Phys. Lett. 89 (2006), 112123 (3 pages).

[19] H.W. Park, M.J. Choi, Y. Jo, K.B. Chung, Low temperature processed InGaZnO thin film transistor using the combination of hydrogen irradiation and annealing, Appl. Surf. Sci. 321 (2014) 520–524.

[20] C.H. Jung, H.I. Kang, D.H. Yoon, The electrical, optical, and structural properties of amorphous indium gallium zinc oxide films and channel thin-film transistors, Solid State Electron. 79 (2013) 125–129.

[21] Y.S. Lee, W.J. Chen, J.S. Huang, S.C. Wu, Effects of composition on optical and electrical properties of amorphous In–Ga–Zn–O films deposited using radio-frequency sputtering with varying O_2 gas flows, Thin Solid Films 520 (2012) 6942–6946.

[22] X.F. Chen, G. He, M. Liu, J.W. Zhang, B. Deng, P.H. Wang, M. Zhang, J.G. Lv, Z.Q. Sun, Modulation of optical and electrical properties of sputtering-derived amorphous InGaZnO thin films by oxygen partial pressure, J. Alloys Compd. 615 (2014) 636–642.

[23] X.F. Chen, G. He, J. Gao, J.W. Zhang, D.Q. Xiao, P. Jin, B. Deng, Substrate temperature dependent structural, optical and electrical properties of amorphous InGaZnO thin films, J. Alloys Compd. 632 (2015) 533–539.

[24] P. Chaudhari, Hillock growth in thin films, J. Appl. Phys. 45 (1974) 4339–4346.

[25] H.C.W. Huang, P. Chaudhari, C.J. Kircher, M. Murakami, Hillock growth kinetics in thin Pb-In-Au films, Philos. Mag. A54 (1986) 583–599.

[26] C.Y. Chang, R.W. Vook, Thermally induced hillock formation in Al–Cu films, J. Mater. Res. 4 (1989) 1172–1181.

[27] F.K. Butt, A.S. Bandarenka, Microwave-assisted synthesis of functional electrode materials for energy applications, J. Solid State Electrochem. 20 (2016) 2915–2928.

[28] S.U. Rehman, F.K. Butt, Z. Tarig, F. Hayat, R. Gilani, F. Aleem, Pressure induced structural and optical properties of cubic phase SnSe: an investigation for the infrared/mid-infrared optoelectronic devices, J. Alloys Compd. 695 (2017) 194–201.

[29] F.K. Butt, B.U. Hag, S. ur Rehman, R. Admed, C. Cao, S. AlFaifi, Investigation of thermoelectric properties of novel cubic phase SnSe: a promising material for thermoelectric applications, J. Alloys Compd. 715 (2017) 438–444.

[30] S.U. Rehman, F.K. Butt, F. Hayat, B.U. Hag, Z. Tarig, F. Aleem, C. Li, An insight into a novel cubic phase SnSe for prospective applications in optoelectronics and clean energy devices, J. Alloys Compd. 733 (2018) 22–32.

[31] F. Ericson, N. Kristensen, J.Å. Schweitz, U. Smith, A transmission electron microscopy study of hillocks in thin aluminum films, J. Vac. Sci. Technol. B9 (1991) 58–63.

[32] D. Gerth, D. Katzer, M. Krohn, Study of the thermal behaviour of thin

aluminium alloy films, Thin Solid Films 208 (1992) 67–75.
[33] C. Kylner, L. Mattsson, Initial development of the lateral hillock distribution in optical quality Al thin films studied in real time, Thin Solid Films 307 (1997) 169–177.
[34] A. Nathan, R.V.R. Murthy, B. Park, S.G. Chamberlain, High performance a-Si:H thin film transistors based on aluminum gate metallization, Microelectron. Reliab. 40 (2000) 947–953.
[35] T.C. Li, M.T. Kao, J.F. Lin, Effects of deposition and annealing conditions on the defects in the Al/glass composites of TFT specimens, J. Mater. Sci. Mater. Electron. 25 (2014) 4425–4433.
[36] J. Zhao, C. He, R. Yang, Z. Shi, M. Cheng, W. Yang, G. Xie, D. Wang, D. Shi, G. Zhang, Ultra-sensitive strain sensors based on piezoresistive nanographene films, Appl. Phys. Lett. 101 (5) (2012), 063112.
[37] Y. Zhang, L. Zhang, C. Zhou, Review of chemistry vapor deposition of graphene and related applications, Accounts Chem. Res. 46 (10) (2013) 2329–2339.
[38] J. Wei, Z. Zang, Y. Zhang, M. Wang, J. Du, X. Tang, Enhanced performance of light-controlled conductive switching in hybrid cuprous oxide/reduced graphene oxide (Cu_2O/rGO) nanocomposites, Opt. Lett. 42 (5) (2017) 911–914.
[39] Z. Zang, X. Zeng, M. Wang, W. Hu, C. Liu, X. Tang, Tunable photoluminescence of water-soluble AgInZnS-graphene oxide (GO) nanocomposites and their application in-vivo bioimaging, Sens. Actuators B Chem. B 252 (2017) 1179–1186.
[40] M.J. Allen, V.C. Tung, R.B. Kaner, Honeycomb carbon: a review of graphene, Chem. Rev. 110 (2010) 132–145.
[41] J.W. Suk, R.D. Piner, J. An, R.S. Ruoff, Mechanical properties of monolayer graphene oxide, ACS Nano 4 (2010) 6557–6564.
[42] C. Baykasoglu, A. Mugan, Nonlinear fracture analysis of single-layer graphene sheets, Eng. Fract. Mech. 96 (2012) 241–250.
[43] R. Dettori, E. Cadelano, L. Colombo, Elastic fields and moduli in defected graphene, J. Phys. Condes. Matter. 24 (2012), 104020 (10 pages).
[44] F. Banhart, J. Kotakoski, A.V. Krasheninnikov, Structural defects in graphene, ACS Nano 5 (2011) 26–41.
[45] S.T. Pantelides, Y. Puzyrev, L. Tsetseris, B. Wang, Defects and doping and their role in functionalizing graphene, MRS Bull. 37 (2012) 1187–1194.
[46] T.C. Li, B.S. Nguyen, Y.C. Chiang, C.L. Hsiao, J.F. Lin, Effects of graphene layers in IGZO/graphite-like+Ni/SiO_2/Si wafer specimens on electrical and optical properties in tribotests, Opt. Mater. Express 6 (2016) 3857–3880.
[47] G.S. Was, Ion beam modification of metal: compositional and microstructure changes, Prog. Surf. Sci. 32 (1990) 221–232.
[48] J. Govaerts, W. Christiaens, J. Vanfleteren, Ultra-thin chip packaging (UTCP): a promising technology for future flexible display interconnection, SID Symp. Digest 40 (2009) 202–205.
[49] X. Li, W. Cai, J. An, S. Kim, J. Nah, D. Yang, R. Piner, A. Velamakanni, I. Jung, E. Tutuc, S.K. Banerjee, L. Colombo, R.S. Ruoff, Large-area synthesis of high-quality and uniform graphene films on copper foils, Science 324 (2009) 1312–1314.
[50] X. Li, L. Colombo, R.S. Ruoff, Synthesis of graphene films on copper foils by chemical, Adv. Mater. 28 (2016) 6247–6252.
[51] M.T. Kao, J.F. Lin, Effects of deposition conditions of the Al film in Al/glass specimens and annealing conditions on internal stresses and hillock formations, Thin Solid Films 520 (2012) 5353–5360.
[52] P.A. Flinn, D.S. Gardner, W.D. Nix, Measurement and interpretation of stress in aluminum-based metallization as a function of thermal history, IEEE Trans. Electron. Dev. 34 (3) (1987) 689–699.
[53] H.P. Klung, L.E. Alexander, X-ray Diffraction Procedures for Polycrystalline and Amorphous Materials, John Wiley & Sons, New York, 1974.
[54] S.H. Jung, H.J. Moon, M.K. Ryu, K.I. Cho, B.S. Bae, E.J. Yun, The effects of high-energy electron beam irradiation on the properties of IGZO thin films prepared by rf magnetron sputtering, J. Ceram. Process. Res. 13 (2012) s246–s250.
[55] J.F. Moulder, W.F. Stickle, P.E. Sobol, K.D. Bomben, Handbook of X-ray Photoelectron Spectroscopy, Perkin-Elmer: Eden Prairie, 1992.
[56] S.J. Kang, J. Baik, H.J. Shin, J.G. Chung, K.H. Kim, J. Lee, X-ray photoelectron spectroscopic investigation of air-annealed amorphous In-Ga-Zn-O thin-film surface electronic and photonic devices, and systems, ECS J. Solid State Sci. Technol. 2 (2013) Q192–Q194.
[57] A. Cánneva, I.S. Giordana, G. Erra, A. Calvo, Organic matter characterization of shale rock by x-ray photoelectron spectroscopy: adventitious carbon contamination and radiation damage, Energy Fuels 31 (10) (2017) 10414–10419.
[58] S. Zhang, Y. Fu, H. Du, X.T. Zeng, Y.C. Liu, Magnetron sputtering of nano-composite (Ti, Cr) CN/DLC coatings, Surf. Coating. Technol. 162 (2002) 42–48.
[59] G. Rajender, P.K. Giri, Formation mechanism of graphene quantum dots and their edge state conversion probed by photoluminescence and Raman spectroscopy, J. Mater. Chem. C. 4 (46) (2016) 10852–10865.
[60] W.N. Miao, X.F. Li, Q. Zhang, L. Huang, Z.J. Zhang, L. Zhang, X.J. Yan, Transparent conductive In_2O_3:Mo thin films prepared by reactive direct current magnetron sputtering at room temperature, Thin Solid Films 500 (2006) 70–73.
[61] V.R. Shinde, T.P. Gujar, C.D. Lokhande, R.S. Mane, S.H. Han, Mn doped and undoped ZnO films: a comparative structural, optical and electrical properties study, Mater. Chem. Phys. 96 (2006) 326–330.